SAN/1196-10

MASTER

HIGH-TEMPERATURE MOLTEN-CARBONATE FUEL CELLS

TECHNICAL PROGRESS REPORT FOR THE PERIOD JULY - SEPTEMBER 1978

B. Baker

D. Burns

D. Dharia

C. Herscovici

A. Leonida

L. Paetsch

P. Patel

A. Pigeaud

C. Shah

J. Yasi

ENERGY RESEARCH CORPORATION
3 Great Pasture Road
Danbury, Connecticut 06810

Date Published - November, 1978

Prepared for the

DEPARTMENT OF ENERGY
20 Massachusetts Avenue
Washington, D.C. 20545

Work Performed Under Contract No. EY-76-C-03-1196

AC03-76ET11304

DISCLAIMER

SAN/1196-10

HIGH TEMPERATURE

MOLTEN CARBONATE FUEL CELLS

TECHNICAL PROGRESS REPORT FOR THE

PERIOD JULY - SEPTEMBER 1978

B. Baker

D. Burns

D. Dharia

C. Herscovici

A. Leonida

L. Paetsch

P. Patel

A. Pigeaud

C. Shah

J. Yasi

ENERGY RESEARCH CORPORATION
3 Great Pasture Road
Danbury, Connecticut 06810

Date Published - November, 1978

Prepared for the

DEPARTMENT OF ENERGY
20 Massachusetts Avenue
Washington, D.C. 20545

Work Performed Under Contract No. EY-76-C-03-1196

EXECUTIVE SUMMARY

Component Development

Pore structures of nickel and nickel-cobalt electrodes were examined by mercury porosimetry and Scanning Electron Microscopy to verify reproducibility of the manufacturing process and to improve their structural compatibility with the other cell components. The manufacturing process for nickel electrodes was scaled for 1500 cm^2 cell testing. The procedures for preparing high surface area nickel-cobalt powder were also scaled from laboratory-size to intermediate-size batches.

Electrolyte powder preparation by the in situ method was scaled from a 3 kg batch to a 6 kg batch and finally to a 10 kg batch. The x-ray difraction and Scanning Electron Microscopic analyses of the intermediate size batch indicated that the lithium aluminate structure is unchanged. Typically, it can be characterized by a predominance of rod-shaped β-$LiAlO_2$ particles of varying size and a minor fraction of clump-like α-$LiAlO_2$ particles.

To improve the electrolyte composition of the powder, five mixtures of alkali carbonates have been selected for further evaluation.

Electrolyte tile manufacturing procedures have also been scaled for 1500 cm^2 cell testing. While this scaling was successful, further work is necessary to improve dimensional tolerances.

The original cell design for studying corrosion of the wet seal area on a cell frame was modified and improved. Attention is focused on the separate measurement of short-circuit and fuel cell currents that flow through this area. Initial measurements on 316 SS indicated that a several-fold reduction in the short-circuit current and a corresponding increase in fuel cell current occurs during the initial life. This is due to the formation

of a barrier film on the outside periphery of the wet seal flange.

Cell Testing

The key results are highlighted below.

- A cell with a nickel-cobalt anode was voluntarily terminated after a stable performance for 3300 hours to examine any structural changes that may have occurred. None were observed in the surface area, mean pore size, porosity and thickness. This establishes the excellent resistance to sintering of the nickel-cobalt anode.

- Good reproducibility of the performance of nickel-cobalt anodes was also observed in a number of laboratory-sized cells. Performance with these higher surface area anodes, as expected, was better than what has been obtained with nickel anodes. The same performance was also observed when the nickel-cobalt anode was scaled to the intermediate sized cells (300 cm^2).

- Lightweight corrugated hardware was tested in an intermediate-sized cell for 1900 hours. Upon termination, no deformation or corrosion of the hardware was observed.

- To arrive at an optimum electrolyte inventory in the electrodes, a comparison of electrode polarization with post-test measurement of electrolyte content in the cell components has begun.

- A diffusion bonded aluminum coating at the wet seal areas of an anode frame provided good corrosion protection in a 3000 hour test.

Modeling and System Analysis

Modeling of cell performance with both nickel and nickel-cobalt anodes was compared. As expected from the difference in their surface areas, a higher value of the overpotential term was obtained for a nickel anode cell compared to that of a nickel-cobalt anode cell.

TABLE OF CONTENTS

		Page No.
	EXECUTIVE SUMMARY	i
TASK 1.	COMPONENT DEVELOPMENT	1
1.1	Electrode Structures	1
1.2	Electrolyte Powder	8
1.3	Electrolyte Tiles	15
1.4	Cell Frame & Current Collector	16
TASK 2.	CELL TESTING	28
2.1	Laboratory-Size Cell Testing	28
2.2	Intermediate-Size Cell Testing	39
2.3	Pilot-Size Cell Testing	44
2.4	Diagnostics	47
TASK 3	STACK DESIGN AND DEVELOPMENT	55
3.1	Sheet Metal Hardware Development	55
3.2	Lightweight Stack Testing	55
TASK 4	MODELING AND SYSTEM ANALYSIS	56
4.1	Cell Performance Modeling	56
4.2	System Study	60
	FUTURE WORK PLAN	63

LIST OF FIGURES

Figure No.		Page No.
1.1.1	Pore Structure of Nickel Electrodes	3
1.1.2	Mean Pore Size vs. Porosity for Nickel Electrodes	4
1.1.3	Pilot-Size (1500 cm^2) Sintered Nickel Plaque	5
1.1.4	Pore Size Distribution for a Nickel and a Nickel-Cobalt Anode	7
1.1.5	Scanning Electron Micrograph for a Nickel and a Nickel-Cobalt Electrode	9
1.2.1	Electron Micrograph of a $LiAlO_2$ Mixture from Batch B-114 (16%α + 80%β + 4%γ)	12
1.2.2	Electron Micrograph of a $LiAlO_2$ Mixture from Batch B-115 (12%α + 81%β + 7%γ)	12
1.2.3	Electron Micrograph of a $LiAlO_2$ Mixture from Scaled-up Batch No IB-1 (11%α + 86%β + 3%γ)	14
1.3.1	1500 cm^2 Electrolyte Tile	17
1.4.1	Electrochemical Cell for Wet Seal Corrosion Studies	18
1.4.2	Effective Current Loops in Dual Electrode Cell	20
1.4.3	Anode Wet Seal Polarization in Absence of Short-Circuit Current With 316 SS	21
1.4.4	Anode Wet Seal Polarization with 316 SS- (after one day of operation)	23
1.4.5	Anode Wet Seal Polarization with 316 SS- (after five days of operation)	24
1.4.6	Local Corrosion and Redox Currents of Anode Wet Seal Area	27
2.1.1	Endurance Characteristics of a Nickel and a Nickel-Cobalt Anode	33
2.1.2	Endurance Test of a Nickel-Cobalt Anode-Cell 118	34

LIST OF FIGURES
(continued)

Figure No.		Page No.
2.1.3	Endurance Testing of Nickel Electrodes-Cell 111	38
2.2.1	Endurance Testing of an Intermediate-size Ni-Co Anode-Cell 7-26	43
2.2.2	Scale-up of a Ni-Co Anode-Cell 110 and 7-26	45
2.2.3	Endurance Testing of a Lightweight Hardware Cell S7-3	46
2.4.1	Electron Micrograph of $LiAlO_2$ of B-112, prior to use in Cell 113 (27%α + 61%β + 12%γ)	54
2.4.2	Electron Micrograph of $LiAlO_2$ of B-112, after use in Cell 113 (36%α + 42%β + 22%γ)	54
4.1.1	Modeling to Explain Parallel Deviation from Experimental Data	59
4.2.1	Schematic of MCFC System	61

LIST OF TABLES

Table No.		Page No.
1.1.1	Manufacture of Nickel Electrodes	2
1.1.2	Ni-Co Electrodes Characteristics-Laboratory Scale Preparation	6
1.1.3	Surface Area, (BET Measurement) of Large Nickel-Cobalt Powder Batches	10
2.1.1	Small Cell Testing--Details of Components	30
2.1.2	Small Cell Testing--Summary of Performance	31
2.1.3	Performance of Nickel-Cobalt Anode Cells	32
2.1.4	Effect of Electrolyte Inventory in Cathode on its Performance	36
2.1.5	Corrosion Protection of Anode Wet Seal Area	40
2.2.1	Intermediate-size Cell Testing--Details of Components	41
2.2.2	Intermediate-size Cell Testing--Summary of Performance	42
2.4.1	Electrolyte Inventory of Cells 104, 113, and S7-2	48
2.4.2	Electrolyte Distribution in the Active Cell Components	49
2.4.3	Stability of Nickel & Nickel-Cobalt Anode	51
2.4.4	Phase Stability of $LiAlO_2$ of Cell 113	53
4.1.1	Modeling Study of Compatibility of Electrodes	57

TASK 1. COMPONENT DEVELOPMENT: C. Herscovici, L. Paetsch, A. Pigeaud and D. Dharia

1.1 Electrode Structures

1.1.1 Electrode Sintering Procedures

300-cm^2 Electrodes: Pore structure characteristics of different nickel electrodes sintered in our hydrogen furnace were examined by mercury porosimetry to verify reproducibility and to improve their structural compatibility. The results are summarized in Table 1.1.1. The pore volume vs. pore size plots are given in Figure 1.1.1. It is seen that the mean pore size decreases with a decrease in porosity. It follows approximately a straight line pattern as shown in Figure 1.1.2.

Our initial effort to make thin cathode structures yielded electrodes with a wide pore size distribution (Batch No 30R, Figure 1.1.1). Further effort will be continued to improve pore structure of thin cathodes.

1500-cm^2 Electrodes: The electrode manufacturing procedures were scaled to make large electrodes for 1500-cm^2 cell testing. A photograph of this large plaque is shown in Figure 1.1.3. Efforts during the next quarter will be concentrated on reducing thickness variations and improving reproducibility.

1.1.2 Stabilized Anode Structures

8.5-cm^2 Electrodes: Characteristics of three Ni-Co electrodes sintered from the two different laboratory scale powder batches are compared in Table 1.1.2. It is clear that the structures are reproducible. A mercury porosimetry curve of a typical Ni-Co anode is compared with a nickel(287) electrode in Figure 1.1.4. It is seen that a Ni-Co anode can be sintered with a smaller mean pore size than that of a Ni anode. It is also interesting to note that the pore volume of the Ni-Co anode is greater than that of the Ni anode. These observations can be explained based on the higher surface area

TABLE 1.1.1

Manufacture of Nickel Electrodes

Electrode Number	Mean Pore Size μ	Porosity %
8R-1	4.4	63
11R-3	7.0	66
30R-9	9.8	71
16R-1	10.0	74

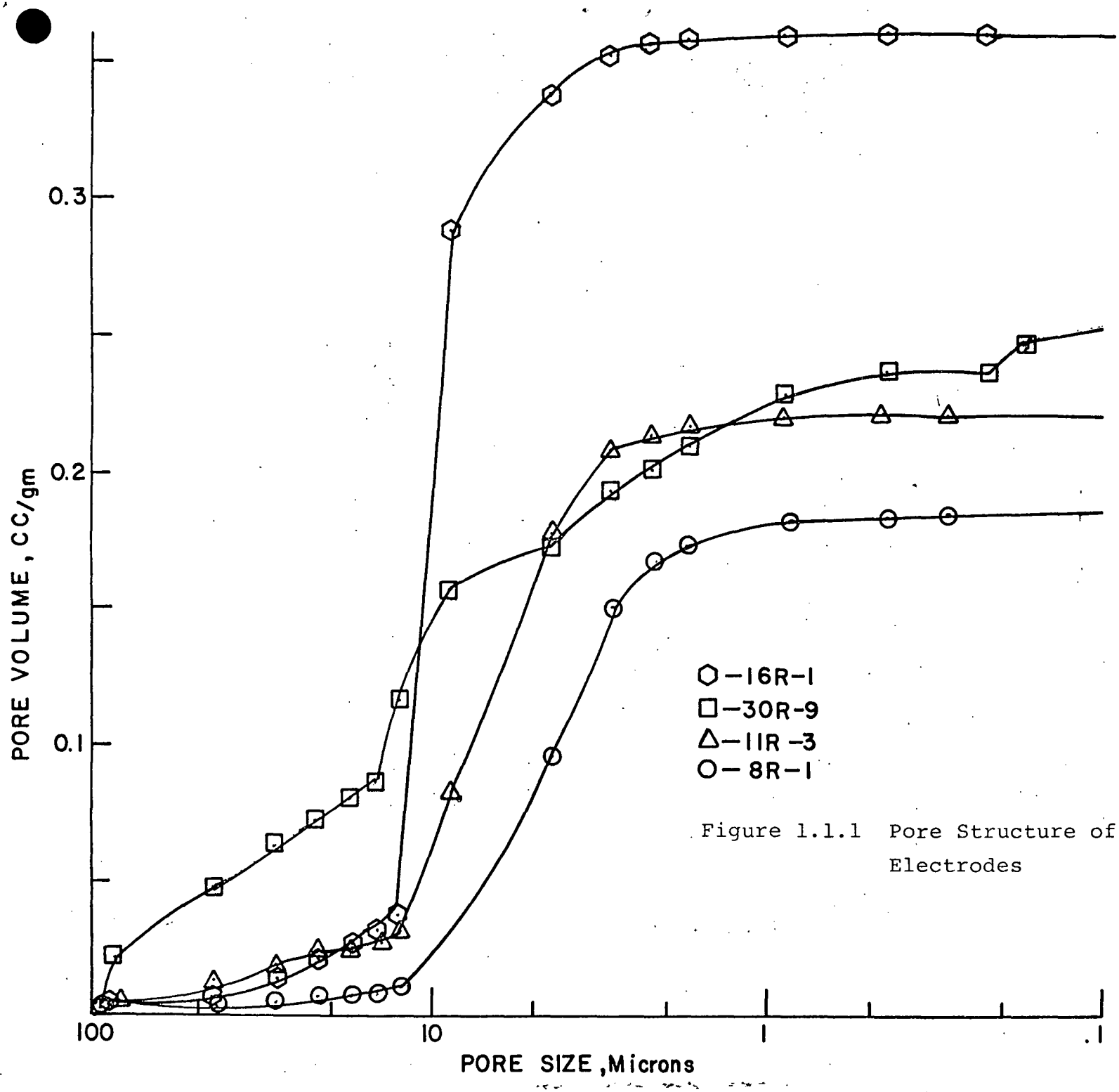

Figure 1.1.1 Pore Structure of Nickel Electrodes

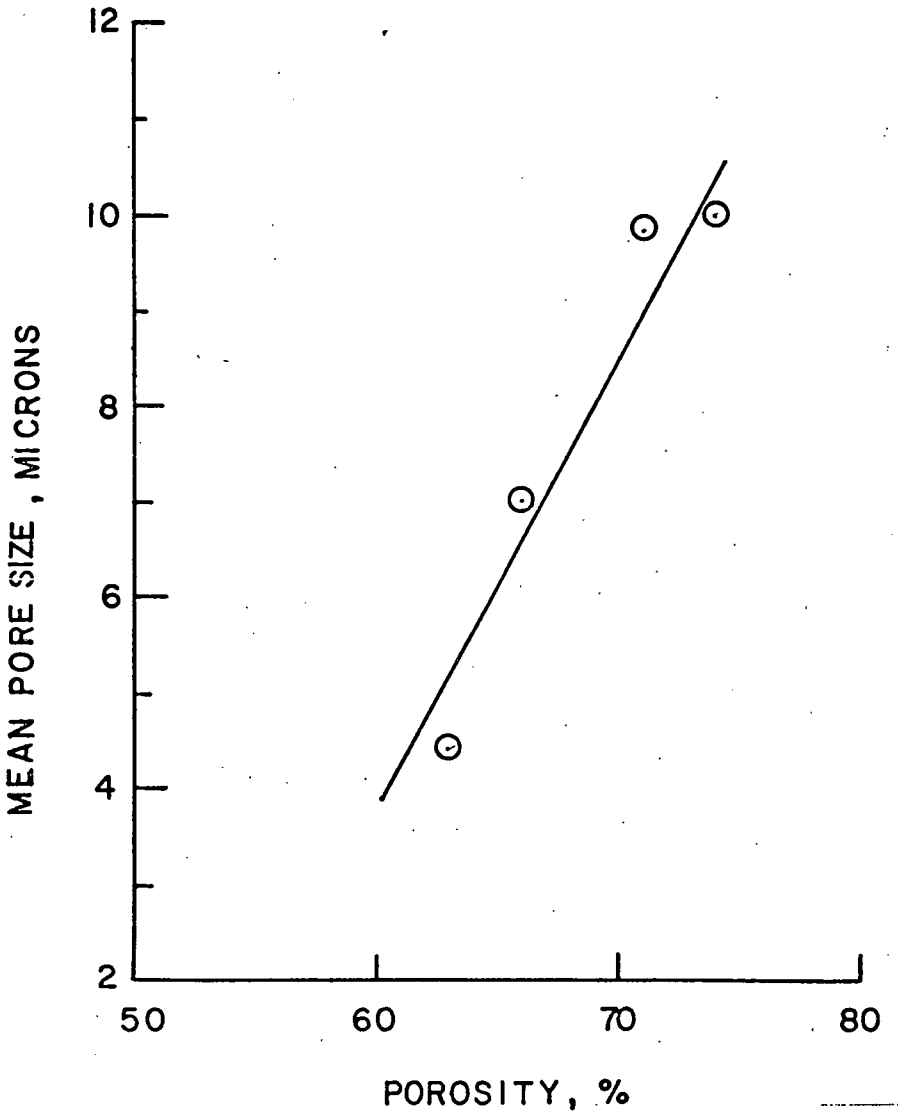

Figure 1.1.2 Mean Pore Size vs. Porosity for Nickel Electrodes

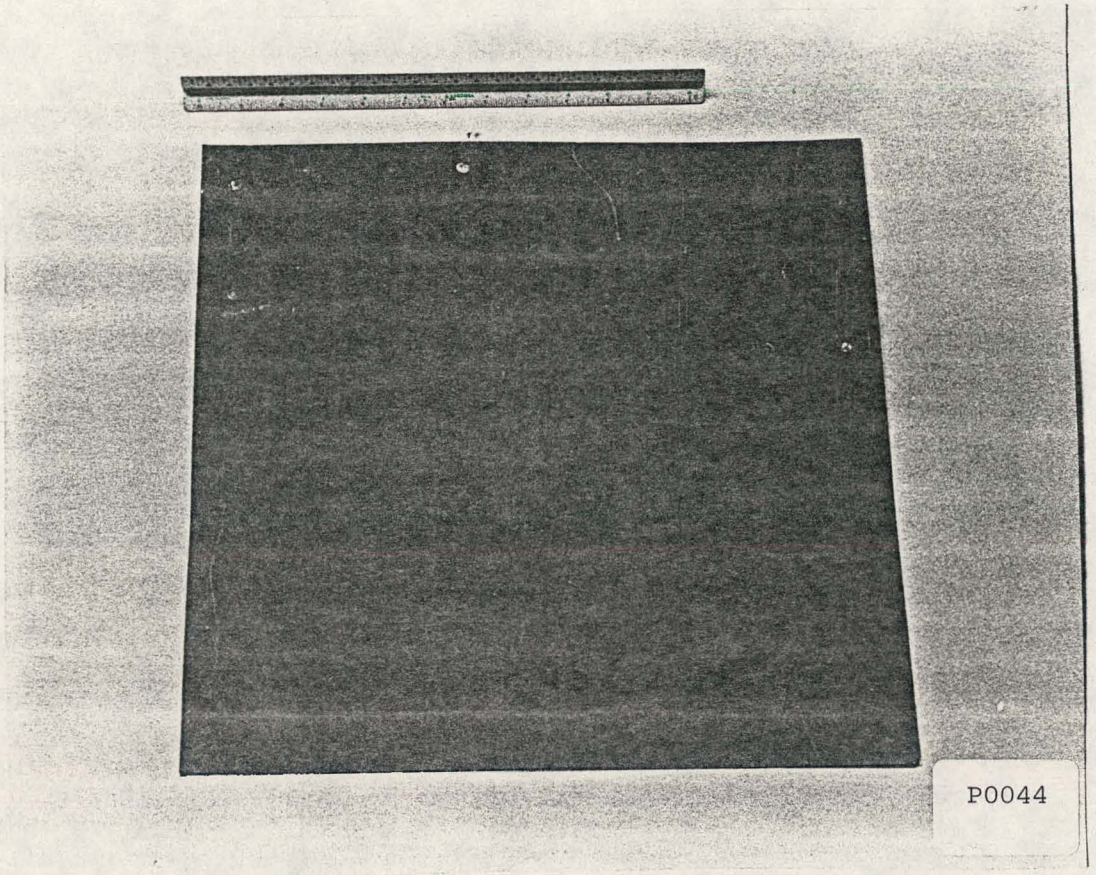

Figure 1.1.3: Pilot-Size (1500 cm^2) Sintered Nickel Plaque.

TABLE 1.1.2

Ni-Co Electrodes Characteristics-

Laboratory Scale Preparation

Batch No.	Thickness Inches	Surface Area m^2/g	Mean Pore Size μm	Porosity %
1	0.025	0.31	2.6	67
2	0.020	0.33	2.7	67
3	0.025	0.34	2.9	70

Figure 1.1.4 PORE SIZE DISTRIBUTION for Ni & Ni-Co ANODE

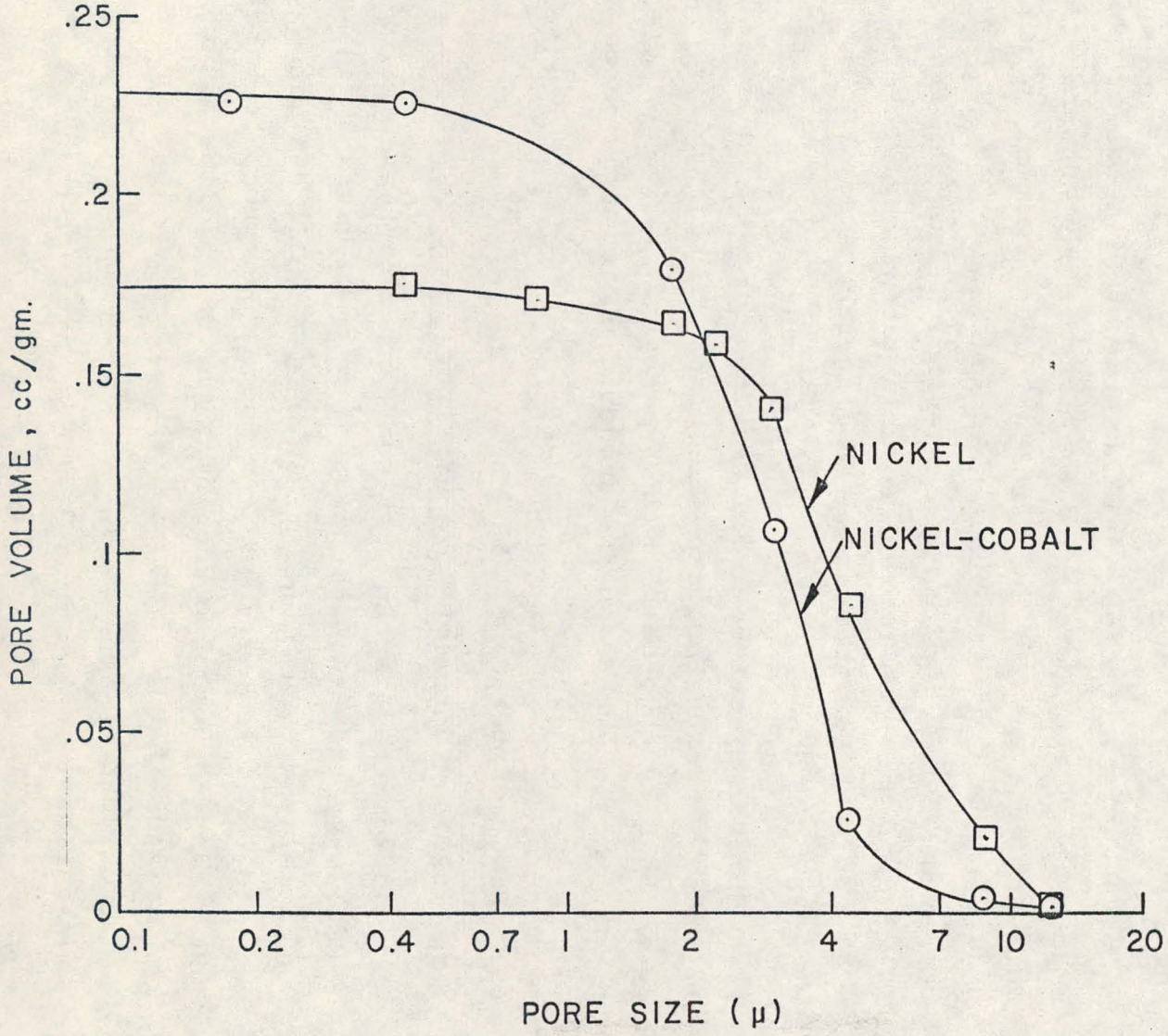

D0227

of the Ni-Co powder, 1.5m^2/g compared to that of the Ni powder, 0.6m^2/g. These observations were further confirmed by comparing their scanning electron micrographs as shown in Figure 1.1.5. It is seen that Ni particles are twice as big in comparison to Ni-Co particles.

300-cm^2 Electrodes: To make larger Ni-Co electrodes, these high surface area powder preparation procedures were scaled. The surface areas of the different powder batches prepared on a larger scale are reported in Table 1.1.3. The surface area of Batch M-905, 1.2m^2/g, is closer to the surface area of 1.5m^2/g of the powder prepared on a laboratory scale. Efforts will be continued to increase the surface area to 1.5m^2/g or more.

Several electrodes were sintered from the above powder batches. As expected, the surface areas of anodes obtained from the first two batches, M-898 and 899, were low (0.1-.14 m^2/g). Measurements on the anodes sintered from batch M-905 are not yet available.

1.2 Electrolyte Powder

1.2.1 Electrolyte Preparation: In Situ Method

As reported in the last Quarterly Progress Report, (No. SAN/1196-9) the $LiAlO_2$ product of in situ Batch B-114 was characterized by a higher yield of β-$LiAlO_2$ (80%) and a well-defined rod-like particle. An increased carbonate particle reduction (-325 mesh powder) was the only deliberate processing change made in B-114. During this reporting period a duplicate electrolyte preparation, No. B-115, was prepared with -325 mesh carbonate powders. The x-ray diffraction and S. E. M. characterization of the $LiAlO_2$ product showed good reproducibility of $LiAlO_2$ phase and particle morphology for B-114 and B-115. Comparative electron micrographs (7500X) of the

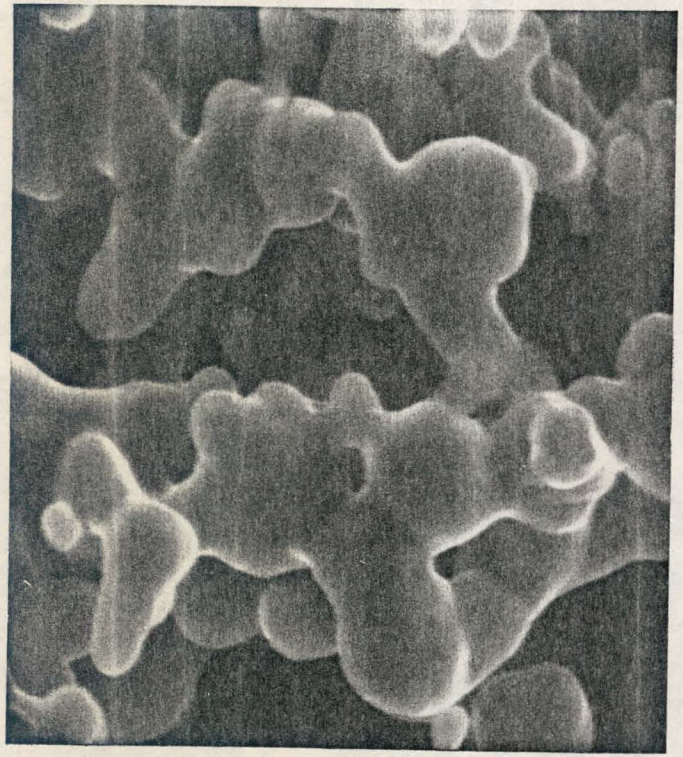

1945-5 8,000X

NICKEL

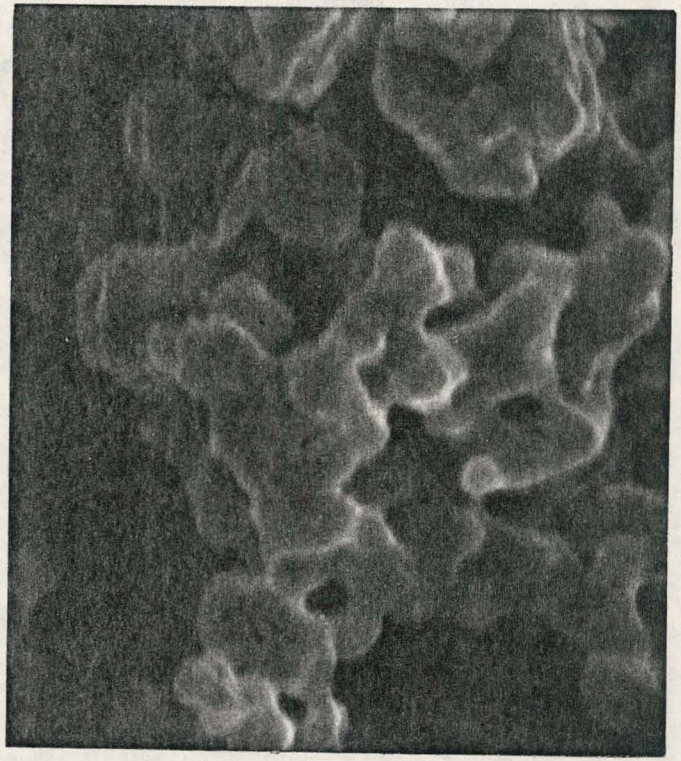

1945-1 8,000X

NICKEL-COBALT

Figure 1.1.5 Scanning Electron Micrographs for a Nickel and a Nickel-Cobalt Electrode

TABLE 1.1.3

Surface Area (BET Measurement) of

Large Nickel-Cobalt Powder Batches

Batch Number	Surface Area m^2/g
M-898	0.24
M-899	0.59
M-904	0.63
M-905	1.21

washed $LiAlO_2$ from Batches B-114 and B-115 are shown in Figures 1.2.1 and 1.2.2 respectively; the phase compositions are indicated in the figure captions. The micrographs show that both products are composed predominately of well-crystallized rods with aspect ratios in the range of 4 to 6, and a minor fraction of clump-like particles. The average particle size of B-115 $LiAlO_2$ appears larger than that of B-114; however, the reason for this apparent difference is not understood. The difference in the BET surface areas of these powders is also in the same direction: B-114 = $4.3 m^2/g$; B-115 = $3.2 m^2/g$.

Future development efforts for the in situ process will be directed towards optimizing carbonate grinding/reagent mixing operations and increasing the product $LiAlO_2$ surface area. More attention will also be directed towards characterization of the pore structure within the $LiAlO_2$ powder. Techniques that produce a small median pore size and a narrow pore size distribution shall be sought.

Preparation of Electrolyte Powder on a Larger Scale: A major portion of the electrolyte development effort during the past quarter centered on the scale up of the in situ process as required to provide for 1500-cm^2 tile fabrication. Processing equipment needed for batch scale up was received and installed. Two intermediate 6 kg batches were prepared (Nos. IB-1, IB-2) and a 10 kg powder batch is currently in preparation.

X-ray and S. E. M. characterization of the $LiAlO_2$ powder from Batch No. IB-1 indicate that the powder is similar to that produced in the smaller 6 kg batches. The $LiAlO_2$ phase composition of the IB-1 was determined to be (11% α + 86% β + 3% γ): this represents a higher yield of β-$LiAlO_2$ than for Batches B-114 and B-115.

The $LiAlO_2$ particle morphology is typically characterized

1921-2 7500X

Figure 1.2.1: Electron Micrograph of a $LiAlO_2$ Mixture from Batch B-114 (16% α + 80% β + 4% γ)

7500X

Figure 1.2.2: Electron Micrograph of a $LiAlO_2$ Mixture from Batch B-115 (12% α + 81% β + 7% γ)

by a predominance of rod-like particles of varying size and a minor fraction of clump-like particles. An electron micrograph (7500X) illustrating the particle morphology of IB-1 is presented in Figure 1.2.3.

1.2.2 Electrolyte Composition Evaluation Study

The majority of the molten carbonate fuel-cell developmental work performed at ERC to date has utilized a standard electrolyte composition of 50 m/o Li_2CO_3 + 50 m/o K_2CO_3. During this quarter, efforts have been initiated to optimize the electrolyte composition of the tile. A fuel-cell testing approach for evaluation of new carbonate compositions will be pursued. The compositions chosen for evaluation are as follows:

1) 50 m/o Li_2CO_3 + 50 m/o K_2CO_3: m.p. = 505°C; this congruently melting mixture has been used in the majority of cell tests to date and will serve as a standard. This mixture represents the compound $LiKCO_3$ and therefore its Li/K ratio is likely to be quite stable. This mixture also represents a good compromise between gas solubility and ionic conductivity in a Li-K binary.

2) 62 m/o Li_2CO_3 + 38 m/o K_2CO_3: m.p. = 488°C; this eutectic mixture has a higher ionic conductivity but a lower gas solubility than our standard.

3) 68 m/o Li_2CO_3 + 32 m/o K_2CO_3: m.p. = 550°C; this higher melting, non-eutectic mixture will be tested to examine the effects associated with high lithium content.

4) 43.5 m/o Li_2CO_3 + 31.5 m/o Na_2CO_3 + 25.0 m/o K_2CO_3: m.p. = 397°C; this low melting ternary eutectic is a good compromise between high ionic conductivity and high gas solubility. Somewhat lower cell operating temperature may be realized with this mixture.

7500X

Figure 1.2.3: Electron Micrograph of a $LiAlO_2$ Mixture from Scaled-up Batch No. IB-1 (11% α + 86% β + 3% γ)

5) 55 m/o Li_2CO_3 + 35 m/o Na_2CO_3 + 10 m/o K_2CO_3: m.p. = 500°C; this non-eutectic ternary mixture has the advantages of high ionic conductivity and low vapor pressure, however the gas solubility is low. Besides evaluating the relative importance of gas solubility in the melt, this mixture will also be used to examine the thermal cycling characteristics of a non-eutectic mixture.

Each of these five compositions has been prepared as a composite powder by physically blending the desired alkali carbonate mixture (as -325 mesh powders) with 45 w/o $LiAlO_2$. A single source of $LiAlO_2$ was used for all the electrolyte compositions so that variations in support structure among the different compositions are minimal. The $LiAlO_2$ was synthesized by the standard in situ method and subsequently washed free of the excess carbonates using acetic anhydride/ acetic acid and absolute methanol as solvents. X-ray analysis of the washed $LiAlO_2$ prior to blending with the various carbonate mixtures indicated a phase composition of approximately 10%α + 80%β + 10%γ $LiAlO_2$.

1.3 Electrolyte Tiles

1.3.1 300 cm^2 Tile Manufacturing

Experiments to eliminate the problem of tile warpage (as described in the last Quarterly Technical Progress Report) were continued. By changing the cooling procedure, the tile warpage has been greatly reduced. Instead of cooling the tile under atmospheric pressure, the change was made to maintain the pressure during the initial period of cooling.

1.3.2 1500 cm^2 Tile Manufacturing

The heater plates for pressing 1500 cm^2 tiles were received. All the components including heater plates, insulation plates, heaters, temperature controller, lifting

device, and roller conveyor were mounted on the press and initial experiments in tile fabrication have begun. The first few experiments yielded tiles of good appearance which either bent or cracked after about 2 to 3 hours. This could be due to residual strain in the tile. By modifying heating procedures, a few tiles have been pressed which are flat. A photograph of this large tile is shown in Figure 1.3.1. However, they still have a thickness variation of $\pm$ 10%. Further experiments will be performed to minimize the thickness variations.

1.4 Cell Frame & Current Collector

1.4.1 Corrosion Current Measurements

Cell Design: The original cell built for wet-seal corrosion studies as introduced in our previous report was modified and improved. A detailed drawing of the final version is presented in Figure 1.4.1. Shown are two identical (1 cm^2) pads of flange material resting on the upper surface of a small electrolyte tile in the bottom of an alumina crucible. The crucible and contents are heated in a small, steelblock furnace held at 650^{o}C.

To simulate the inner edge of an anode wet-seal, one of the pads is placed within a slightly larger diameter alumina tube capable of surrounding the pad with the required fuel atmosphere. The other pad which then simulates the outer edge of the same wet seal is held in an ambient atmosphere as desired (e.g., mixtures of air, CO_2, N_2, O_2, etc.). The two 1/16"-thick pads can be connected by means of spotwelded leads to a 1Ω shunt which then allows a continuous short-circuit current to flow between the two pads. This current represents the uninterrupted electron flux between the inner and outer surfaces of a wet seal flange. It can be monitored by means of a millivolt electrometer placed across the 1Ω shunt as shown

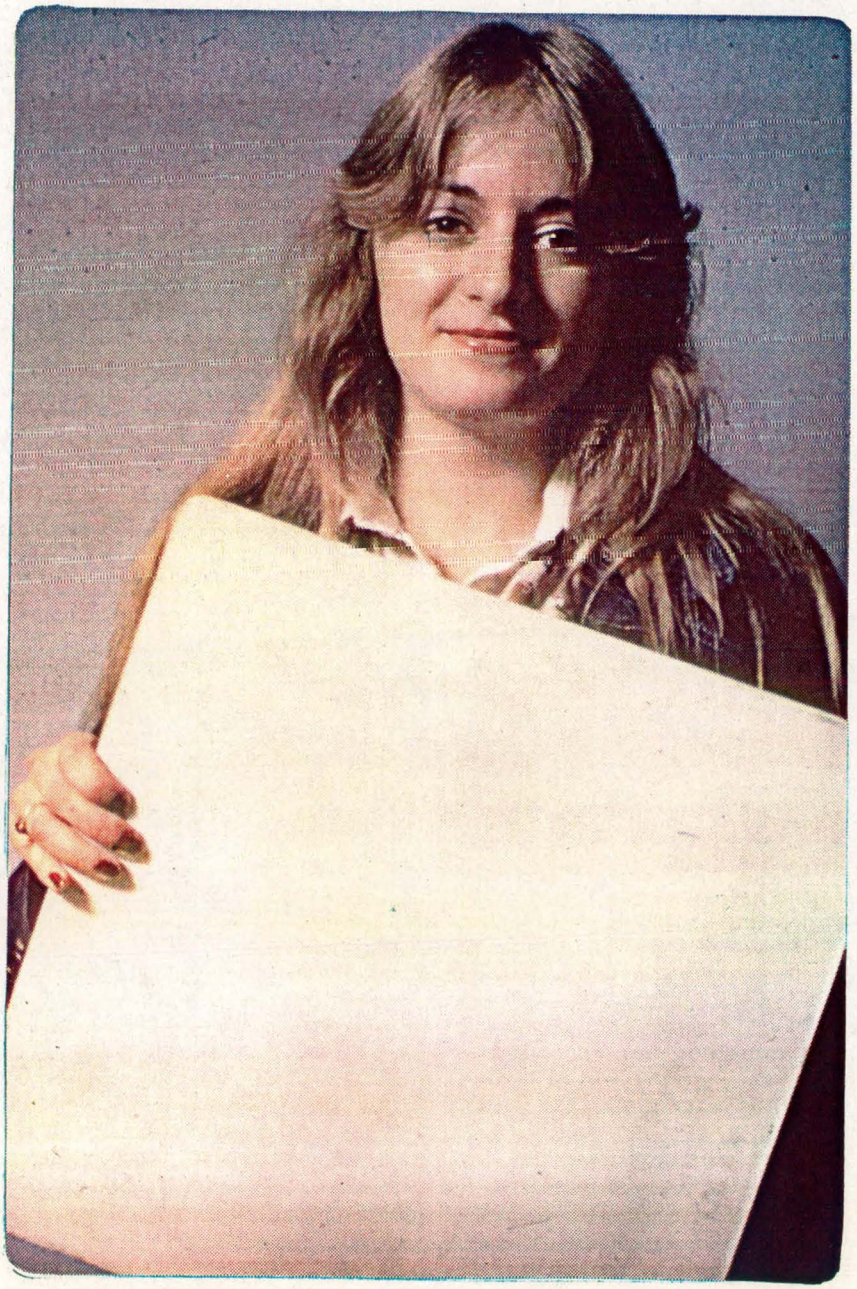

Figure 1.3.1: 1500 cm^2 Electrolyte Tile

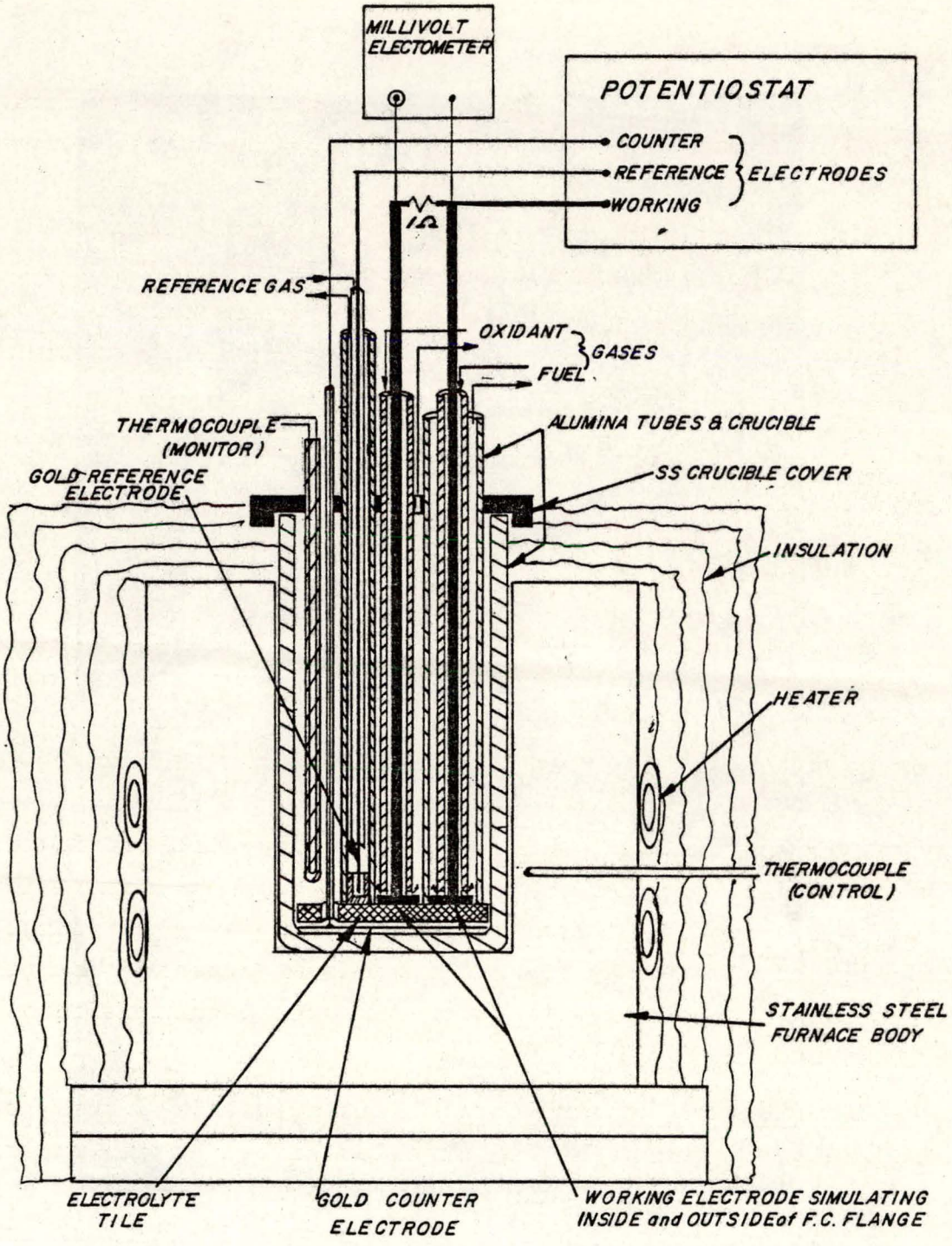

FIG. 1·4·1 — ELECTROCHEMICAL CELL
for WET SEAL CORROSION STUDIES

DO 268

in the figure.

The dual-electrode assembly thus formed is also connected to a potentiostat which, by means of a gold counter electrode underneath the tile, controls the combined potential of the assembly with respect to a standard reference electrode ($Au/O_2/2CO_2$) that touches the top of the tile. Thus, the wet seal area of an anode frame, which is commonly the most severely attacked region in a fuel cell, may be adequately simulated with this apparatus.

Figure 1.4.2 summarizes the current loops to be considered in this cell configuration. The dotted loop in the center of the figure represents short-circuit current (i_1) flowing between the inside and outside surfaces of a wet seal flange.

The heavy, solid loop shown around the perimeter of the figure represents the normal fuel cell current (i_2) flowing between the anodic and cathodic parts of a cell. In an operating fuel cell, this should represent a very small fraction of the cell's total current. By proper selection of inner and outer electrode gas mixtures, the above cell configuration can be used to examine the relationship between fuel oxidation and metal corrosion currents at the anode wet seal flange. Also, the effects of coating the anode wet seal area and changing the outside gas composition with respect to this relationship will be examined.

Experimental Measurements: Initial work reported here has been performed using 316 stainless steel as the material for both the electrode pads. Figure 1.4.3 illustrates the initial polarization behavior (i_2^o vs. E) of the fresh inner pad when it is not connected to the outer (oxygen-supplied) pad. An initial OCV = -1005 mV was obtained which is close to the theoretical value of the particular fuel/reference

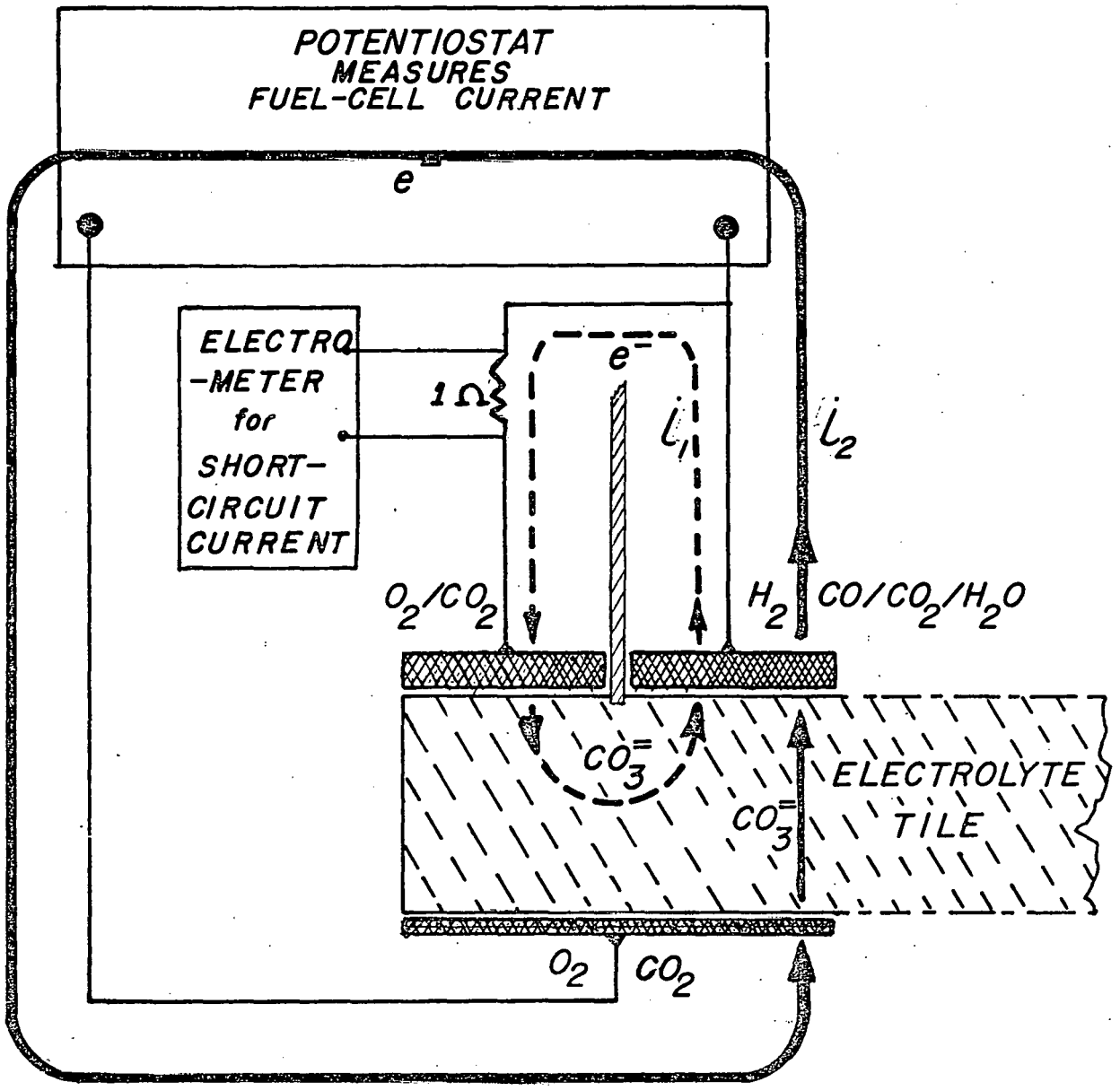

FIG. 1·4·2 , EFFECTIVE CURRENT LOOPS In
DUAL ELECTRODE CELL

DO 269

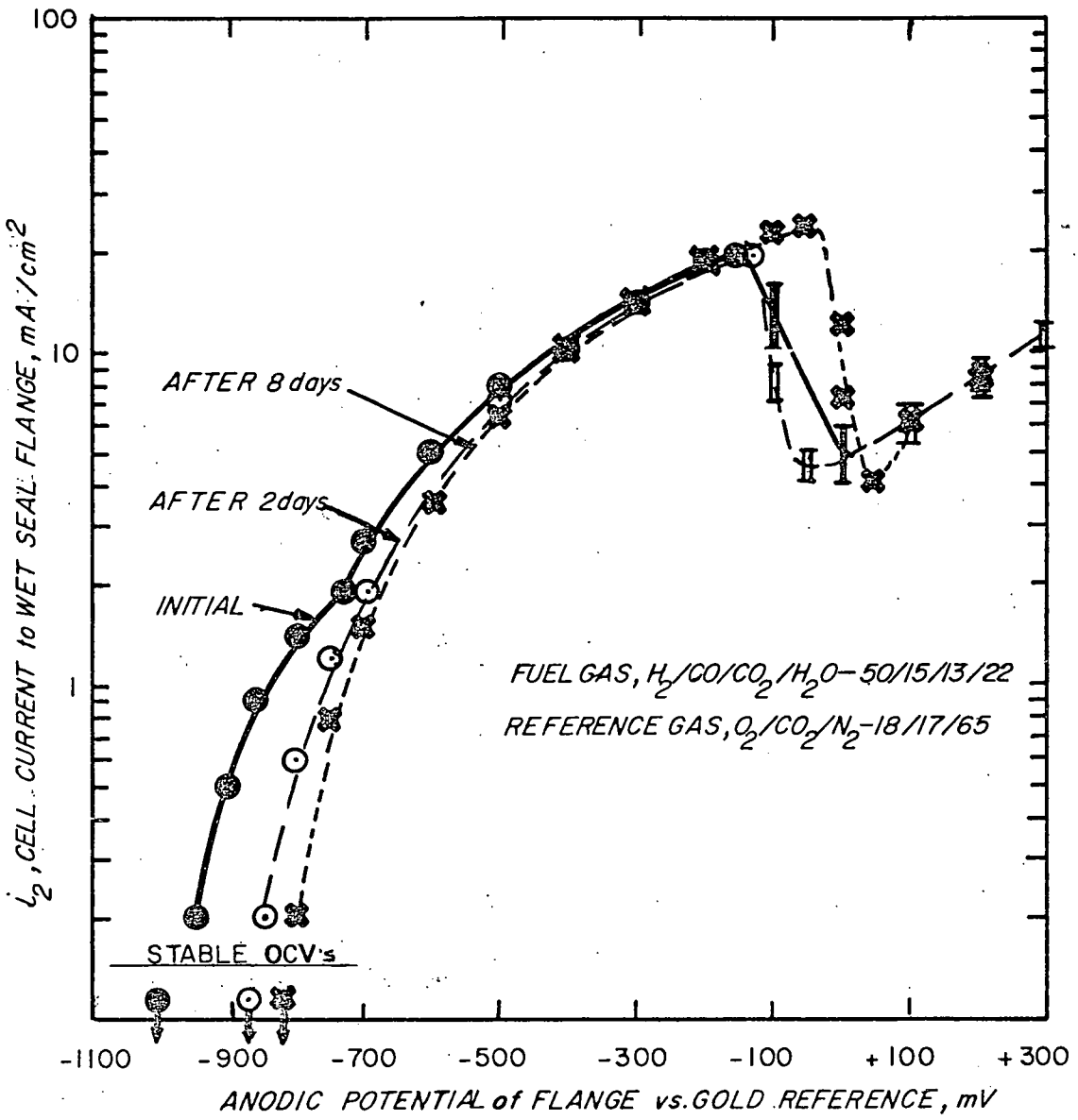

Figure 1.4.3 Anode Wet Seal Polarization in Absence of Short-Circuit Current with 316 SS

DO 270

gas combination used.

Our first measurements were made with a non-standard reference ($18O_2/17CO_2/65N_2$). Polarization data was also obtained after 2 and 8 days of operation of the cell. During the in-between periods, the cell was operated with the 1Ω shunt closed and only for base-line measurements was the shunt disconnected. E vs I data was obtained by the isopotential, chronogalvametric technique which allows for extended stabilization periods of the corrosion current under different overvoltage conditions.

The first curve obtained shows a small initial current wave which is typically associated with the first stages of anodic film formation. This and the general shift of both the OCV's and the polarization curves toward more positive values as time elapses (and as current is drawn through the electrodes) is interpreted as formation of an increasingly more stable oxide barrier film on the inner electrode surface.

Even though the overvoltage region from -1000 to -700mV is the only one of interest in studying the anode wet seal behavior, more positive potentials are applied in our studies of wet seal materials and coatings to characterize them under more severe conditions such as may be expected in a multicell stack. Accordingly, flange potential minima are found as shown in Figure 1.4.3 between -100 and 0 mV anodic potential. Interestingly, these minima also shift toward more positive values indicating that in the given reducing atmosphere, passive films also form in addition to oxide barrier films.

The next set of measurements obtained after 1 and 5 days of operation (Figures 1.4.4 and 1.4.5) show the cell currents, i_1 and i_2, with the electrode assembly being polarized with the 1Ω shunt connected. A large short-curcuit current, i_1,

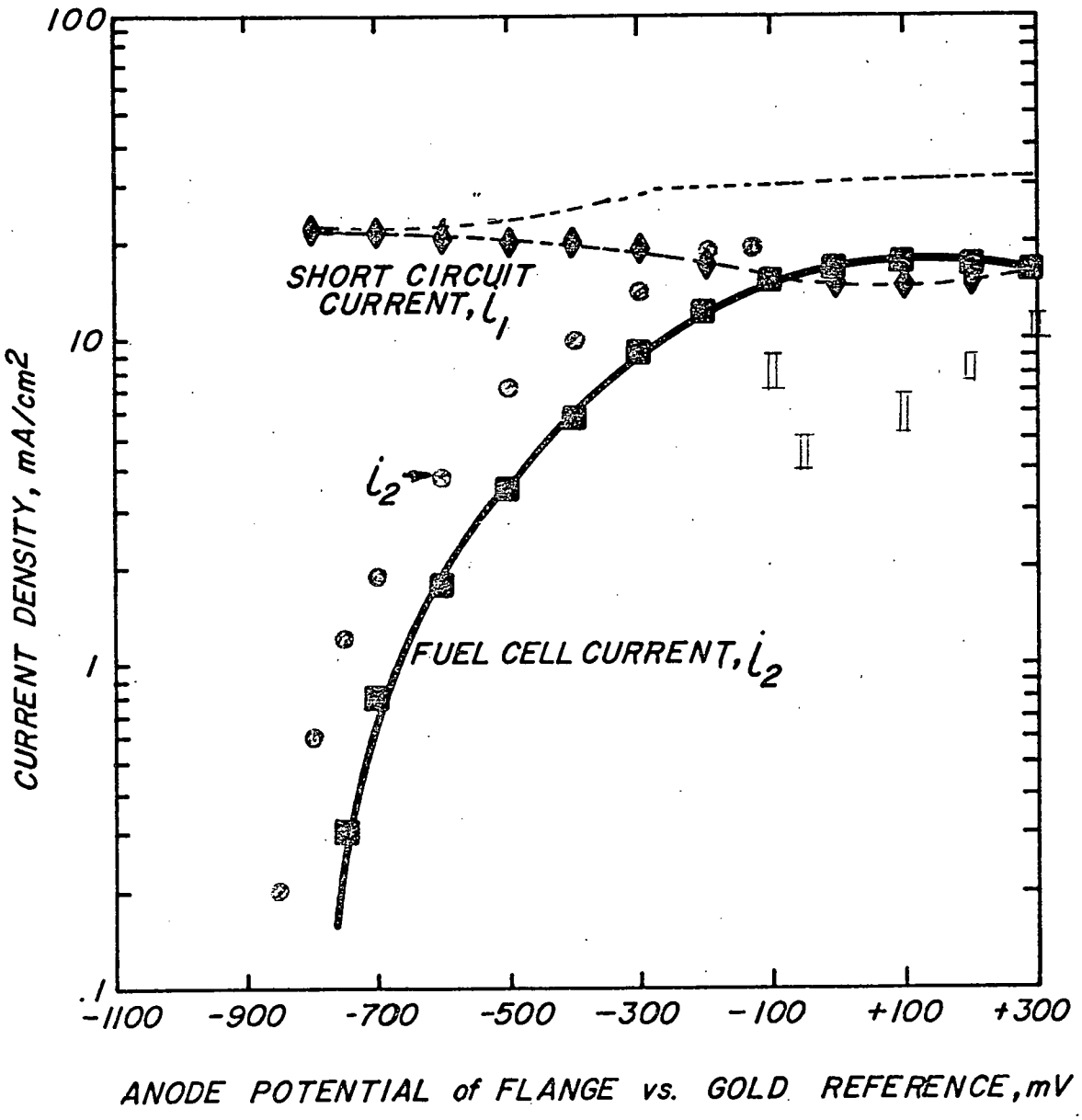

Figure 1.4.4 Anode Wet Seal Polarization with 316 SS (after one day of operation)

DO 271

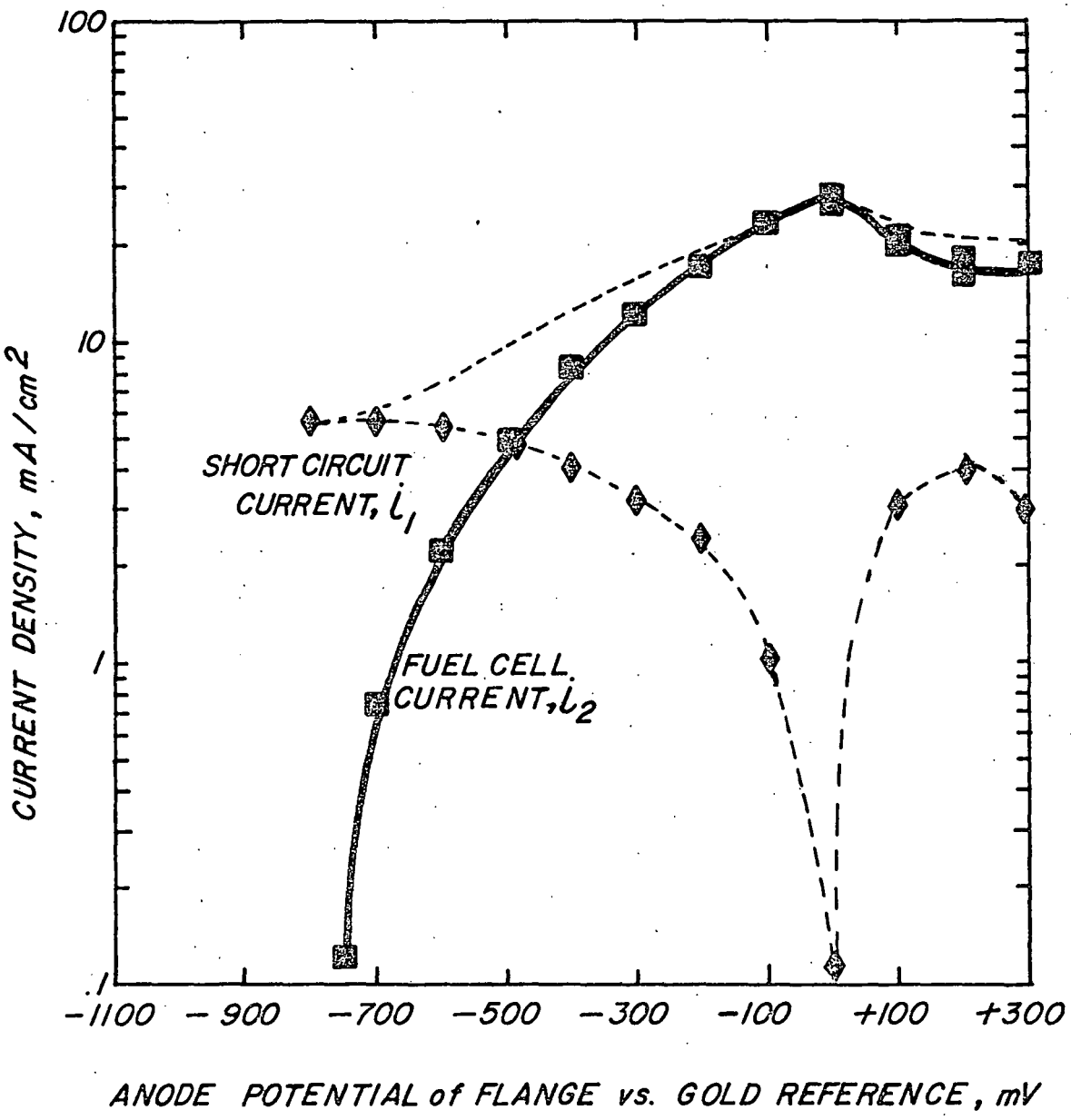

Figure 1.4.5 Anode Wet Seal Polarization with 316 SS (after five days of operation)

now flows continuously between the two electrodes at all times. This is in addition to the fuel cell current, i_2, conducted by the inside electrode while the assembly is polarized with the potentiostat. Baseline values after two days, i^o_2, from Figure 1.4.3 are also shown in Figure 1.4.4 for comparison purposes.

Figure 1.4.4 shows that the inner edge polarization as measured by the fuel cell current, i_2, is shifted further toward positive potentials. This is due to the additional short-circuit current i_1, being also drawn through the fuel electrode. The total current, $i_1 + i_2$, varies from 22 to a maximum of 32 mA/cm^2 as the potential is made more positive. This increase is due to increases in fuel cell current while the short-circuit current decreased from 22 to 15 mA/cm^2.

After five days of operation with inner and outer pads connected, however, polarization behavior is significantly different. The fuel cell current, i_2, supplies a larger fraction of the total current than before while the short-circuit current, i_1, has now been reduced several fold with a passive minimum at 0 mV anodic potential. Because of this, the total current in Figure 1.4.5 starts at a much lower level. A passive film clearly has formed on the outer electrode since the total current (the major portion of which is due to fuel cell current, i_2) still increases to almost 32 mA/cm^2 when the electrode assembly is polarized in the positive direction. It is certain that the history of current flow through the wet seal area greatly affects the processes of polarization and corrosion. Additional measurements and analyses are necessary to interpret this behavior accurately.

Discussion: The summary of effective current loops illustrated in Figure 1.4.2 readily shows that two processes are taking place which are somewhat offset in time. Initially, the inner edge electrode is fairly rapidly oxidized leading to a rapid change in OCV but not a large increase in resistance. Next, the outer edge electrode is oxidized but more slowly and this leads to a large increase in resistance as is indicated by the much lower short circuit currents shown in Figure 1.4.5.

Consideration should also be given to local corrosion behavior at the anode wet seal surface. Figure 1.4.6 shows a schematic of the current distribution where the wet seal is in contact with the tile. For simplicity, the interactions with the cathode flange are not shown. At the inner vertical edge of the anode flange, the local oxidation current is supplied primarily by hydrogen while at the outer vertical edge, the local reduction current is supplied by O_2/CO_2. At the tile/metal contact face, however, where the concentrations of gaseous species are low, it is the metal itself which supplies the oxidizable species. Thus, most, but not all short-circuit current, i_1, is corrosion current. Also, current-density used in metal oxidation is clearly much greater toward the outer than the inner edge because of the shorter path for $CO_3^=$ ion flow. This closely corroborates our actual observations in operating fuel cells where the most severe undercutting of metal is experienced at the outer edge of the anode flange.

In summary, studies with the present cell are providing an understanding of the complex interactions between the fuel cell currents and the parasitic (partly corrosion) currents present in a wet seal area. Further measurements with variable gas atmospheres and different alloy materials and coatings are in progress.

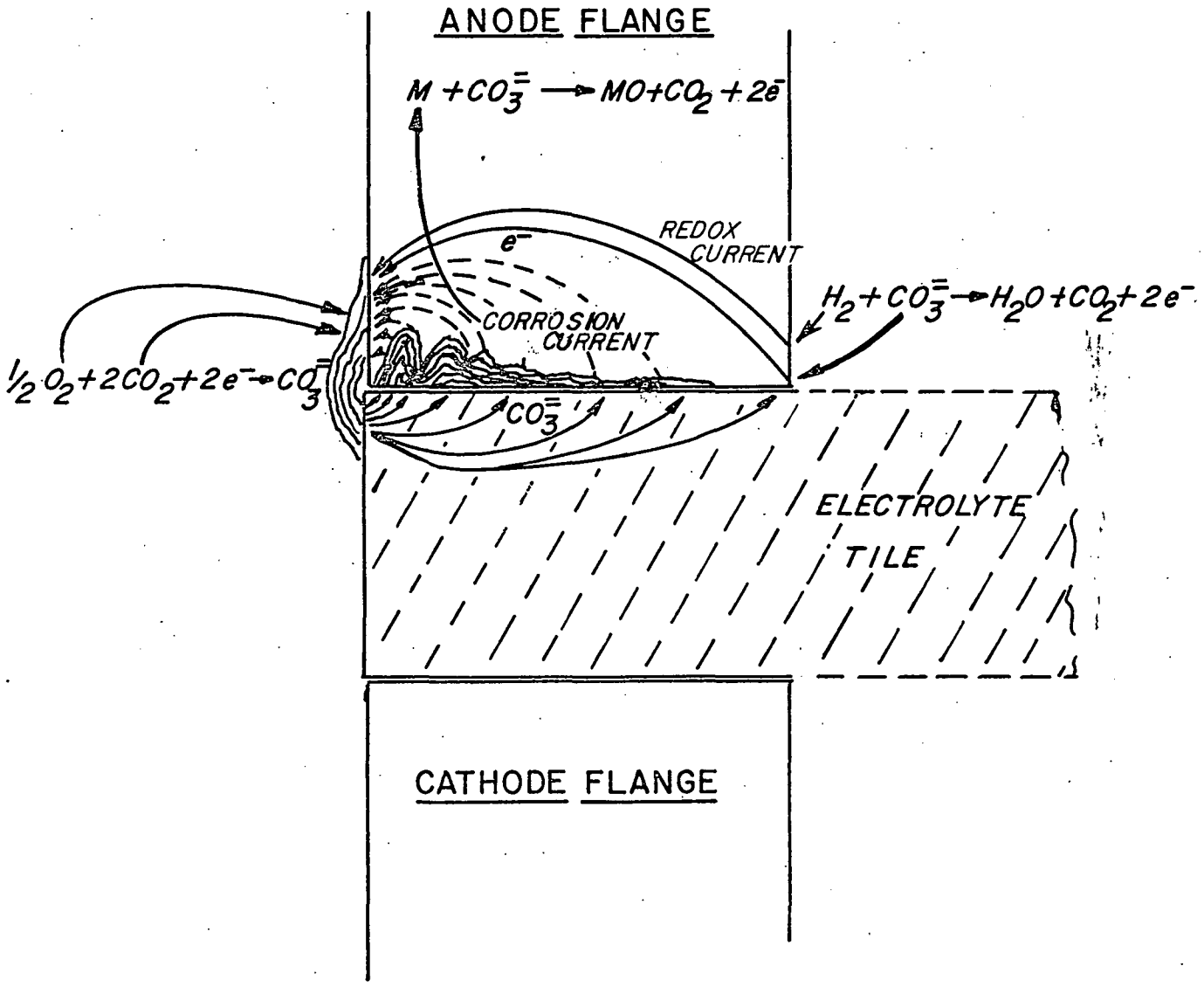

FIG. 1·4·6 - LOCAL CORROSION and REDOX CURRENTS at ANODE WET SEAL AREA

DO 273

TASK 2: CELL TESTING: A. Leonida, J. Yasi, C. Shah, P. Patel and D. Dharia

The main areas investigated during the present quarter are:

a) Establishing stable performance with nickel-cobalt anode cells and their scale-up

b) Testing lightweight sheet metal hardware

c) Analyzing the electrolyte inventory of the electrodes and its effect on cell overpotential, and

d) Examining the stability of lithium aluminate structures in fuel cells.

So far, three small cells have exceeded 3000 hours of endurance having either a nickel anode (Cell 104 and 111) or a nickel-cobalt anode (Cell 110). The first two cells with a nickel anode displayed a performance decay near the end of the test while the latter with a nickel-cobalt anode showed no drop in performance. A large cell with a nickel-cobalt anode has displayed a steady performance for 1200 hours with the test continuing (Cell 7-26). Lightweight sheet metal hardware was endurance tested for 1900 hours. No deformation in the structure of the hardware was observed. The scale-up to 1500 cm^2 (15" X 15" cell) has been initiated. Work has begun to analyze the effect of electrolyte inventory of the electrodes. These results are described in Sections 2.1 to 2.4 below.

2.1 Laboratory-Size Cell Testing

Efforts in the laboratory-size cell testing were concentrated toward evaluating performance reproducibility of stabilized anodes and endurance testing of nickel and nickel-cobalt anode cells. Preliminary analysis was made to relate polarization at an electrode with its electrolyte inventory.

Tables 2.1.1 and 2.1.2 present a summary of these tests.

2.1.1 Stabilized Anode Structures

Endurance testing of nickel-cobalt anodes continued through the present quarter (Cells 110 and 118). Table 2.1.3 compares the performance of various nickel-cobalt anode cells. The IR-free cell potential of the Cells 110 and 118 at 117 mA/cm^2 was close while a 30 mV higher performance was observed for Cell 112 which was due to more compatible cathode structure as explained in the previous report.

Cell 110, was voluntarily terminated after 3300 hours of endurance to examine the anode structure. As can be seen from Figure 2.1.1, the performance was stable throughout the cell life. No appreciable decay was observed in the OCV and the wet seal efficiency and the cell resistance was almost constant. Figure 2.1.1 illustrates performance stability of the nickel-cobalt anode as compared to a nickel anode. Both Cells 104 and 110 have all other components the same except the anodes. The nickel anode cell showed a decay in performance after 1500 hours, whereas the performance of Cell 110 was stable.

Structural stability of the nickel-cobalt anode from Cell 110 was examined with respect to thickness, mean pore size, porosity and surface area. As described in Section 2.4, the anode displayed an excellent sintering resistance.

Cell 118, with both the anode and the cathode of Ni-Co alloy, displayed stable performance for 1100 hours of cell life (Figure 2.1.2). However, an unplanned thermal cycle resulted in a small decay in OCV and wet seal efficiency. The test was discontinued after 1700 hours of endurance. The performance of the cell was comparable to that of Cell 110 as explained above. However, resistance of Cell 118 was higher

TABLE 2.1.1 SMALL CELL TESTING - DETAILS OF COMPONENTS

CELL NO.	ELECTRODES						ELECTROLYTE					PURPOSE OF CELL TEST
	ANODE			CATHODE								
	Thickness (mil)	Mean Pore Size (µm)	Porosity (%)	Thickness (mil)	Mean Pore Size (µm)	Porosity (%)	Composition	Batch No.	Tile Density (g/cc)	% of Theoretical Density	Thickness of Tile (mil)	
113	26.5	4.2	69.4	20.5	10	74.5	STD*	B-112	2.38	96	83	Large electrolyte batch with 27% α-$LiAlO_2$
117	26.5	4.2	69.4	22	10	82.8	STD	KI-1	2.44	96	77	Electrolyte made by aqueous slurry method
118	22	2.6	65.7	25	2.9	73.3	STD	B-108	2.43	96	83	Ni-Co electrode at both anode and cathode
121	20	2.6	65.0	16	2.7	76	STD	B-108	2.40	95	78	Performance of a thin cathode and endurance stability of Ebrite as c.c. material
122	30	6.4	66.4	14	9.0	73.4	STD	B-112	2.49	99	70	Ni-Co anode sintered from powder manufactured in the scale-up batches
123	27	6.4	65.0	14	10.0	74.5	STD	B-114	2.40	97	80	To evaluate large electrolyte batch (B-114) with electrode pair being same as in Cell 122

*STD Composition is 55% liquid electrolyte ($LiKCO_3$) and 45% sclid lithium aluminate

TABLE 2.1.2

SMALL CELL TESTING - SUMMARY OF PERFORMANCE

CELL NO.	ENDURANCE (hrs)	IR CORRECTED VOLTAGE AT 1A (117 mA/cm^2) (V)	R (mΩ)	WET SEAL EFFICIENCY (Exit gas flows as % of inlet)		COMMENTS
				ANODE	CATHODE	
111	288	0.747	108	98	98	The cell having nickel electrodes displayed good wet seal efficiencies and stable ohmic resistance with average performance.
	533	0.809	90	99	92	
	1005	0.763	82	92	98	
	1530	0.657	71	100	100	
	2000	0.691	71	100	100	
	2478	0.736	80	86	95	
	3000	0.610	165	86	100	
113	98	0.841	79	82	93	Cell displayed good performance for 200 hours which then decreased, indicating a significant structural change in cell compartments.
	339	0.682	90	90	95	
	652	0.688	97	100	98	
	1207	0.688	108	95	100	
	1608	0.685*	260	90	95	
117	45	0.629	240	85	97	The cell displayed low performance and high resistance; on termination a contact problem was revealed on the cathode side.
	279	0.683	80	94	98	
	449	0.749	190	95	100	
	759	0.661*	300	87	100	
118	26	0.818	108	98	100	Initial performance of the cell is comparable to Cell 110 having similar components except the cathode. The cell performance dropped following an accidental thermal cycle.
	218	0.883	82	94	100	
	707	0.854	94	85	100	
	1045	0.792	52	82	100	
	1214	0.815	108	51	97	
	1550	0.809	139	45	96	
	1692	0.725	128	58	95	
121	93	0.814	133	100	95	The ohmic resistance of the cell having a thin cathode is higher than expected. Probably the cathode protrusion is not enough to insure good contact.
	162	0.755	56	100	99	
	354	0.797	105	94	96	
	520	0.767	43	96	97	
	685	0.626	206	90	94	
122	47	0.716	105	94	99	Initial performance of the cell is low, probably due to low surface area of the Ni-Co anode made by the scale-up method.
	286	0.699	115	96	93	
123	21	0.681†	150	100	99	The cell with electrolyte tile made from B-114 displayed high resistance and poor performance. However, the wet seals are good.
	164	0.650	150	91	95	
	355	0.716	180	100	100	

*At 94 mA/cm^2

†All data points at 94 mA/cm^2

TABLE 2.1.3

PERFORMANCE OF NICKEL-COBALT ANODE CELLS

Cell No.	Cell Resistance m Ohms	Cell Potential at 117 mA/cm^2* m Volts	IR Free Cell Potential at 117 mA/cm^2 m Volts
110	68	780	848
112	49	814	863
118	87	766	853
7-26	4	700	820

*At standard composition and flows

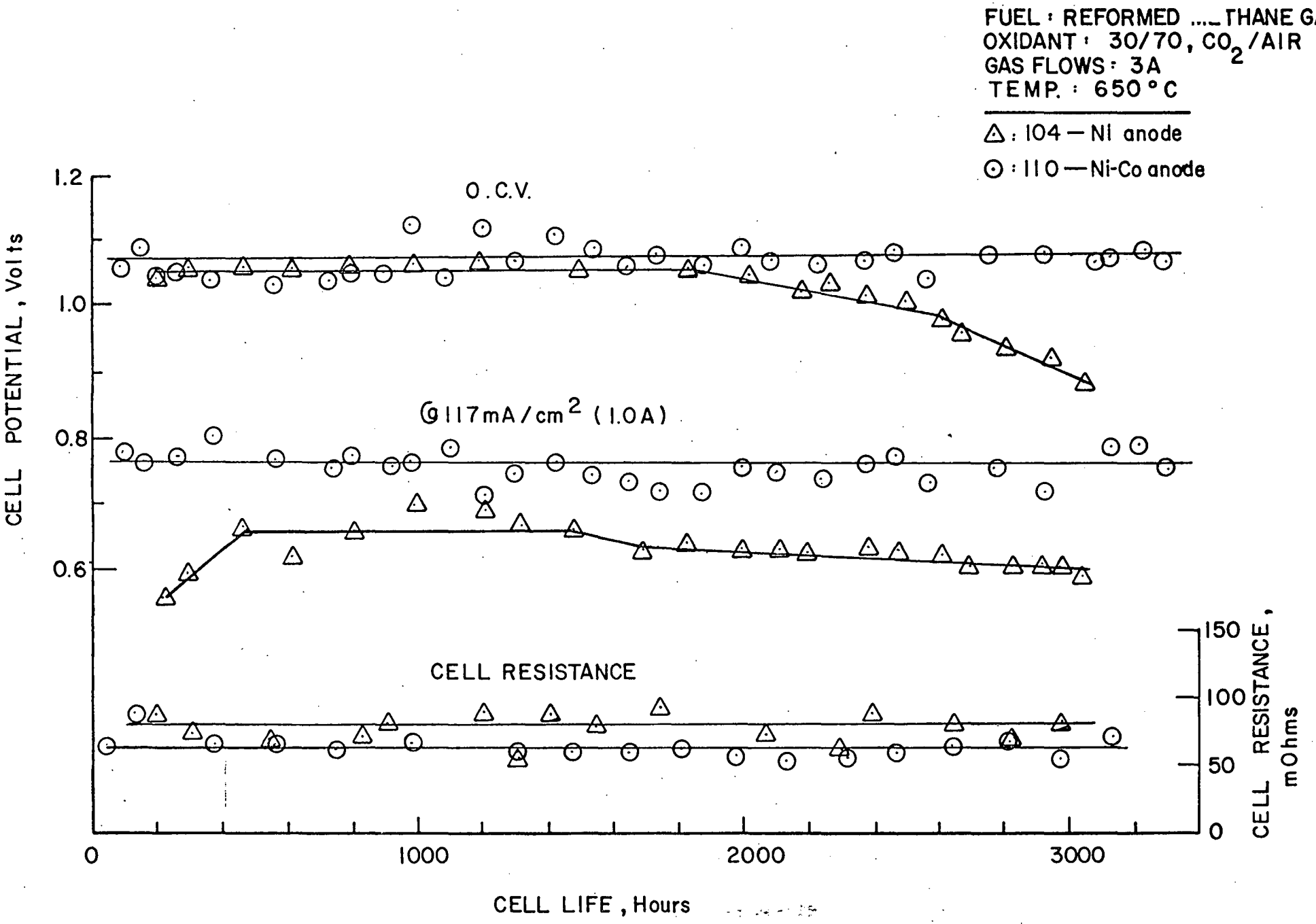

Figure 2.1.1 ENDURANCE CHARACTERISTICS of NICKEL & NICKEL-COBALT ANODES

D0228

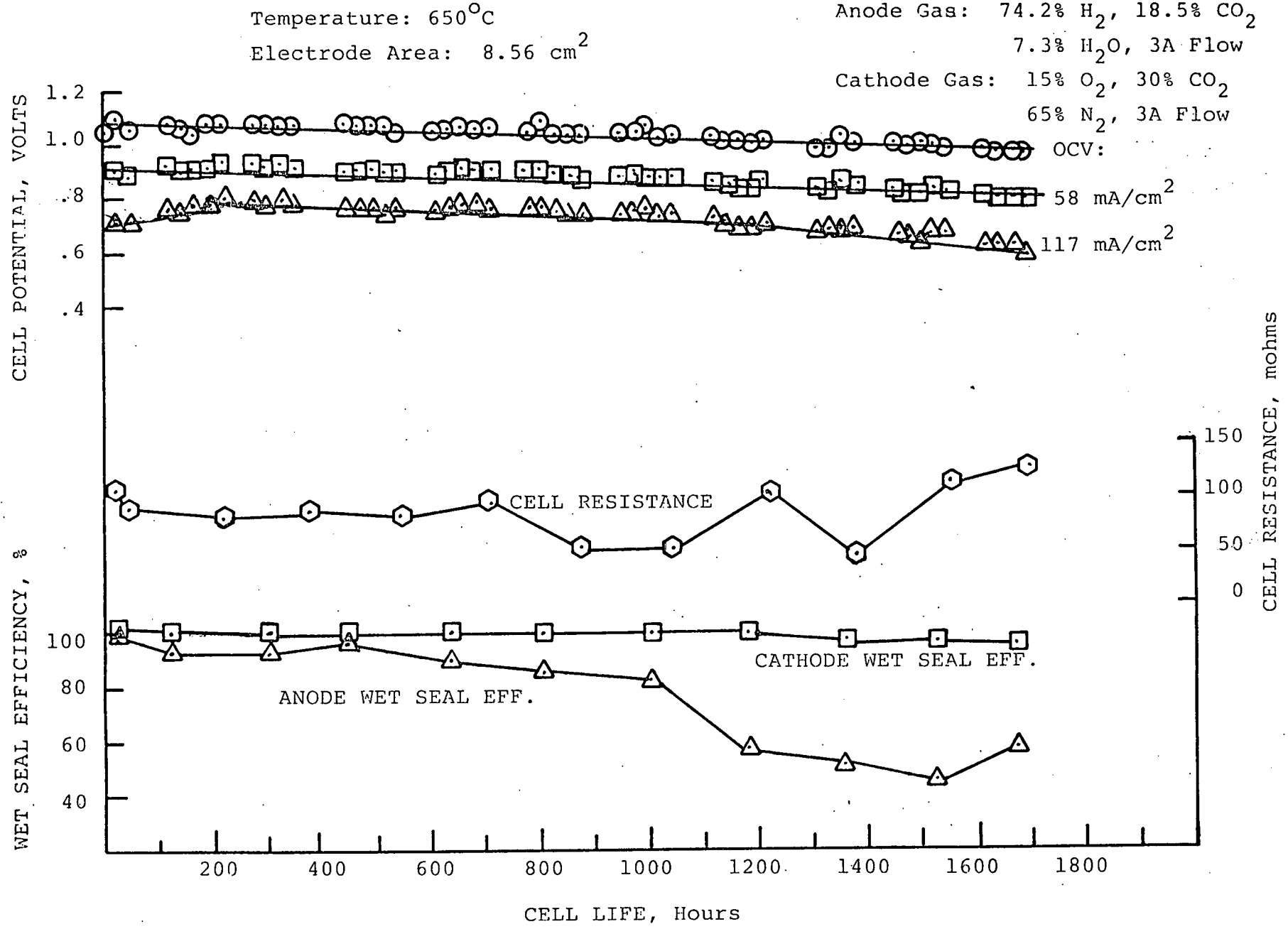

Figure 2.1.2, Endurance Test of a Ni-Co Anode - Cell 118

by about 15 mΩ. This could be explained by the thicker cathode structure of Cell 118 as compared to Cell 110. Apparently, high surface area at the cathode did not improve the cell performance.

Cell 121, having a nickel-cobalt anode, was started to evaluate the performance of a thin cathode. However, a contact problem on the cathode was revealed. The test will be repeated with better design of the cathode frame to suit thin cathodes.

Cells 122 and 123 have been started with Ni-Co anodes sintered from a large powder batch, as described in Section 1.1.1. The initial performance of these cells is lower than that of Cell 110. Both of the cells also exhibited higher resistance, probably due to the improper design of the cell frame for thin cathodes as mentioned above. The BET surface area measurements revealed that the anode surface area is in the range of 0.1-0.14 m^2/g compared to 0.31 m^2/g for the anode of Cell 110. As discussed in Section 1.1.1, the larger scale process needs further improvement.

2.1.2 Compatibility of the Cell Components

Influence of anode and cathode pore structure compatibility on cell performance was described in the previous Quarterly Technical Progress Reports (SAN/1196-8 and 9). A study has been initiated to relate the electrolyte inventory of the electrodes with their respective polarizations.* For a qualitative analysis, the percentage of pore volume of electrode occupied by the electrolyte was used to characterize the inventory. As shown in Table 2.1.4, an interesting relationship between cathode polarization and the cathode inventory was revealed. The cathodes with large electrolyte contents

*As characterized by a O_2-CO_2 gain or a performance loss with H_2 lean Fuel

TABLE 2.1.4

EFFECT OF ELECTROLYTE INVENTORY IN CATHODE ON ITS PERFORMANCE

Cell No.	% of Cathode Pore Volume Occupied by Electrolyte	O_2-CO_2 Gain at 117 mA/cm^2
7-17	100	200
104	44	105
110	47	100
112	25	70

displayed higher O_2-CO_2 gains. Reduction of cathode inventory from 100 percent in Cell 7-17 to 50 percent in Cell 104 resulted in an improvement of 95 mV in the observed values of O_2-CO_2 gains. However, a further reduction to 25% inventory of cathode yielded an additional improvement of 35 mV only. This type of analysis is useful to arrive at an optimum electrolyte content in the electrodes. At present, sufficient data for anode inventories are not available to establish a trend.

2.1.3 Endurance Testing

Last quarter, the endurance test of Cell 104 for 3100 hours was described. Post-test measurements for this cell are discussed in Section 2.4. During the present quarter, two more cells accumulated 3000+ hours of endurance (Cell 111 and 110). As planned earlier, the tests were discontinued to provide data for stability of cell components and electrolyte distribution.

Cell 111 assembled with nickel electrodes accumulated 3100 hours of endurance with stable performance for 2300 hours. The life-graph for this cell is presented in Figure 2.1.3. A small drop in the performance observed after 2700 hours can be explained by a combined effect of OCV and an increase in ohmic resistance. The wet seal efficiencies were good and constant throughout the cell life. Post-test measurements showed that the thickness change in the nickel anode was approximately 4 mils. The nickel-oxide cathode separated itself in two halves, one sticking to the tile and the other to the cathode current collector. The anode frame was brittle and corroded. However, this corrosion didn't affect anode wet seal efficiency. A large amount of carbonate creepage was observed on the anode frame and support.

Temperature: 650°C

Electrode Area: 8.56 sq. cm.

Anode Gas: 74.2% H_2, 18.5% CO_2, 7.3% H_2O, 3A Flow

Cathode Gas: 15% O_2, 30% CO_2, 55% N_2, 3A Flow

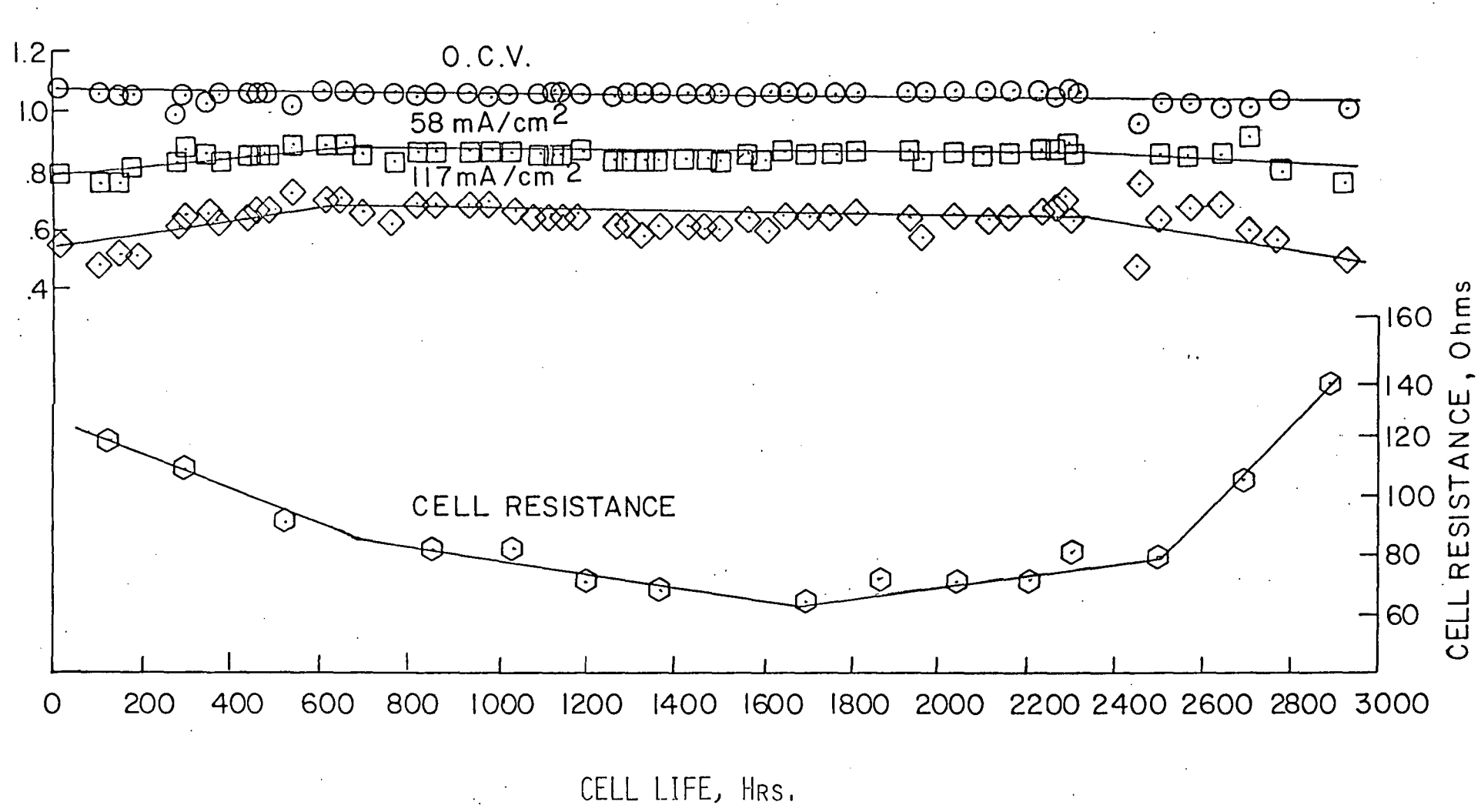

Figure 2.1.3 Endurance Testing of Nickel Electrodes - Cell 111

D0265

Endurance testing of Cells 110 and 118 having nickel-cobalt anodes has been discussed in Section 2.1.1. In general, these cells displayed more stable performance than the nickel-anode cells.

2.1.4 Corrosion Study

The effect of various forms of seals for corrosion protection of gas seal area was discussed in an earlier report (SAN/1196-7, page 39). During the present quarter, a similar analysis was made for relatively longer life cells. As expected, on the cathode side comparatively low corrosion was observed. However, corrosion of the anode frame depended greatly upon the form of the seal and the electrolyte creepage. As shown in Table 2.1.5, the best protection was obtained for a diffusion bonded aluminum coating.

2.2 Intermediate-Size Cell Testing

Efforts in the intermediate-size cell testing were directed towards evaluating the scale-up of the stabilized anode structure and different configurations for the light-weight hardware cells.

Component details for the intermediate-size (300 cm^2) cell tests conducted this quarter are presented in Table 2.2.1 and their performance is compared in Table 2.2.2. Performance evaluation of these tests is discussed below.

2.2.1 Stabilized Anode Structure

A 300 cm^2 cell (Cell 7-26) having a Ni-Co anode was started this quarter to scale up the stable performance observed in 8.56 cm^2 cells. As can be seen from Figure 2.2.1, performance of the cell is quite stable for the first 1200 hours of endurance. So far, the wet seal efficiencies and OCV have shown no decay and the test is continuing.

TABLE 2.1.5

CORROSION PROTECTION OF ANODE WET SEAL AREA

CELL NO.	TYPE OF CORROSION PROTECTION	CELL ENDURANCE HOURS	REMARKS ON POST TEST OBSERVATIONS OF ANODE WET SEAL AREA	
			Appearance	Apparent Mechanical Strength
104	Aluminum gasket	3100	Corroded, porous, somewhat sharp edges	brittle
110	Diffusion bonded aluminum coating	3300	Good. No corrosion, sharp edges	good
111*	Aluminum coating	3100	Corroded, porous and blunt edges	brittle
112	Diffusion bonded aluminum coating	1500	Good. No corrosion, sharp edges	good

* For this cell, a large electrolyte creepage was observed on the anode frame.

TABLE 2.2.1 INTERMEDIATE-SIZE (300 cm^2) CELL TESTING - DETAILS OF COMPONENTS

CELL NO.	ELECTRODES						ELECTROLYTE					PURPOSE OF CELL TEST
	ANODE			CATHODE								
Thickness	Thickness (mil)	Mean Pore Size (μm)	Porosity (%)	Thickness (mil)	Mean Pore Size (μm)	Porosity (%)	Composition	Batch No.	Tile Density (g/cc)	% of Theoretical Density	Thickness of Tile (mil)	
S7-3	27	4.2	65.1	20	10	72.6	STD*	B-112	2.50	98	75	Lightweight frames with SS screen reinforced cathode and no mechanical support
S7-4	27	4.2	69.5	21	10	74.6	STD	B-114	2.43	98	63	To test straight pattern lightweight hardware at cathode (DIGAS cooling)
7-26	17	4.0	69.7	16	9.8	71	STD	B-112	2.43	97	70	Stability of Ni-Co anode and thin cathode in large cell. Electrolyte addition to anode chamber
7-27	26	7.3	74.4	20	10	70.9	STD	B-114	2.40	98	98	Compatibility of electrolyte structure with a tested pair of electrodes

*STD composition is 55 Wt % liquid carbonates and 45% solid lithium aluminate.

TABLE 2.2.2 INTERMEDIATE-SIZE (300-cm^2) CELL TESTING - SUMMARY OF PERFORMANCE

Cell No.	Endurance (hrs)	IR Corrected Voltage at 1A (117 mA/cm^2) (V)	R (mΩ)	Wet Seal Efficiency (Exit gas flows as % of inlet)		Comments
				Anode	Cathode	
S7-3	72	0.728	5.6	98	84	The lightweight hardware cell having new structure at the cathode and no mechanical support displayed higher performance than that of Cell S7-2. The cell also exhibited longer endurance.
	381	0.810	3.7	91	91	
	787	0.820	3.9	67	92	
	1217	0.806	5.2	54	100	
	1456	0.649	2.2	49	100	
	1721	0.554	8.8	61	87	
	1871	0.548*	6.0	65	18	
7-26	19	0.833	9.0	94	90	As expected, the first 300-cm^2 cell having Ni-Co anode displayed stable and good performance for 1300 hours. The test is continuing.
	523	0.863	5.5	97	92	
	697	0.744	2.2	90	99	
	865	0.849	5.6	93	100	
	1004	0.805	4.9	95	97	
	1194	0.824	5.6	93	97	
7-27†	23	0.614	18	100	97	The cell has good wet seal efficiencies but low performance due to high ohmic resistance. The current collector was found warped on termination.
	258	0.775	20	99	97	

*At 94 mA/cm^2

†At 37 mA/cm^2

Temperature: 650°C
Electrode Area: 271 cm^2
Anode Gas: 74.2% H_2, 18.5% CO_2
7.3% H_2O, 100A Flow
Cathode Gas: 15% O_2, 30% CO_2, 55% N_2
100A Flow

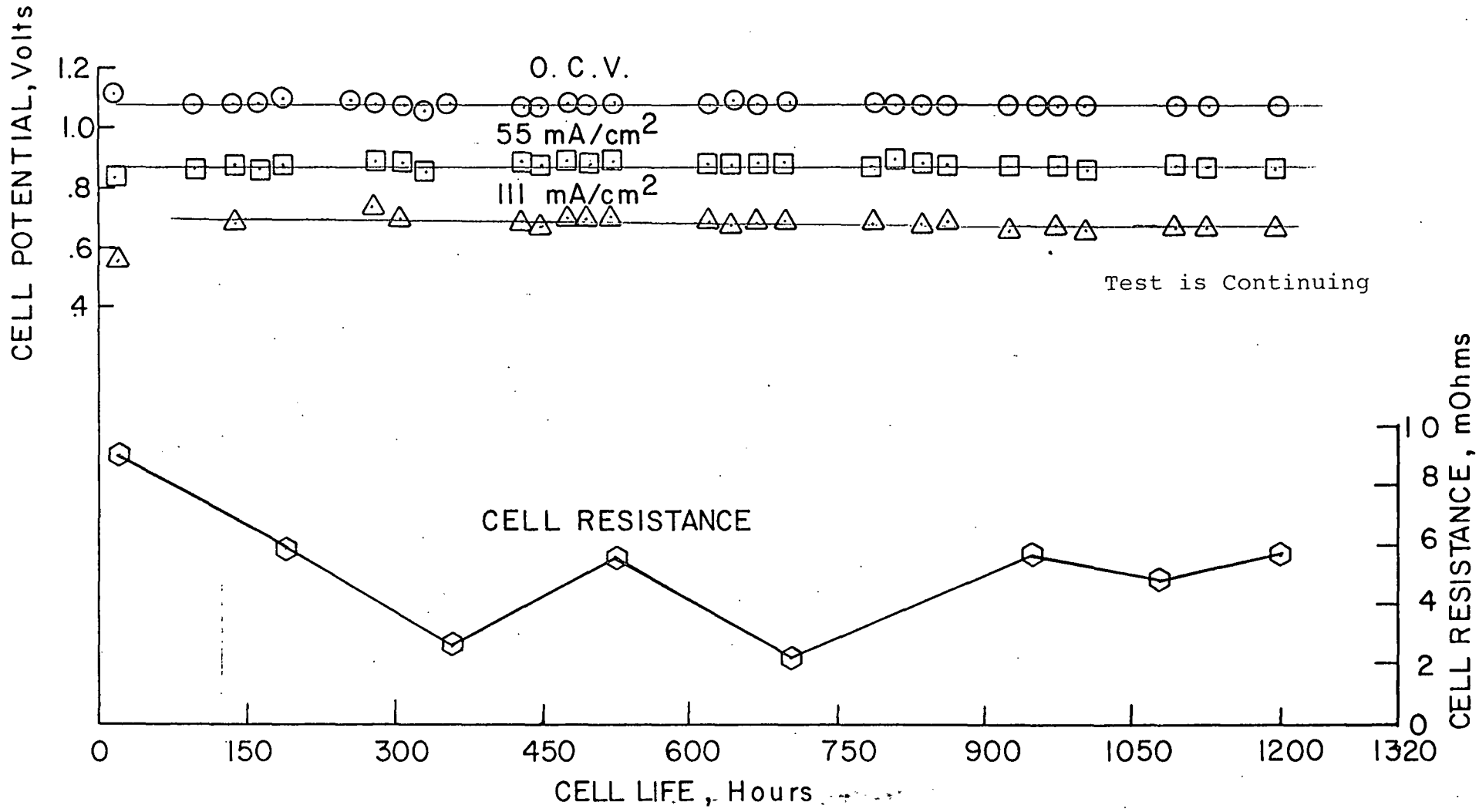

Figure 2.2.1. Endurance Testing of an Intermediate-Size (300-cm^2) Ni-Co Anode - Cell 7-26

Figure 2.2.2 compares the performance of small Cell 110 having a Ni-Co anode with the large cell (7-26). The IR-corrected performance of the scale-up is quite comparable with the small cell. However, the ohmic overpotential in Cell 7-26 is larger than that of Cell 110. Insufficient expansion of the thin cathode used in the cell could be the cause for the higher resistance.

2.2.2 Lightweight Hardware Testing

Cell S7-3, started last quarter, has a staggered pattern lightweight sheet metal frame for both the electrodes. As shown in Figure 2.2.3, Cell S7-3 accumulated 1900 hours of endurance. However, after 900 hours of stable performance, the anode wet seal efficiency indicated a small decay. This was reflected in the loss of performance. During post-test analysis, the sheet metal hardware was found intact and apparently there was no change in the height of the corrugations. This established a good structural stability for the lightweight hardware.

It was described in the last report that Cell S-7-4 didn't exhibit good performance from the beginning and had very high resistance. Upon termination, a poor contact of the cathode was noted. This explained the observed high resistance and low cathode wet-seal efficiency. This was caused by an uneven expansion of the corrugated sheet metal and the supporting frame. The test will be repeated with an improved cathode frame design.

2.3 Pilot-Size Cell Testing (1500 cm^2)

Testing of 300 cm^2 cells will be scaled up to 1500 cm^2 cells. Control panel and press have been designed and constructed for this task. Design of the cell frame and auxilliaries is completed and currently the parts are being

Temperature: 650°C
Anode Gas: 74.2% H_2, 18.5% CO_2
7.3% H_2O
Cathode Gas: 15% O_2, 30% CO_2, 55% N_2
Cell 110: Electrode Area: 8.56 cm^2
Gas Flows: 3A
Cell 7-26: Electrode Area: 271 cm^2
Gas Flows: 100 A

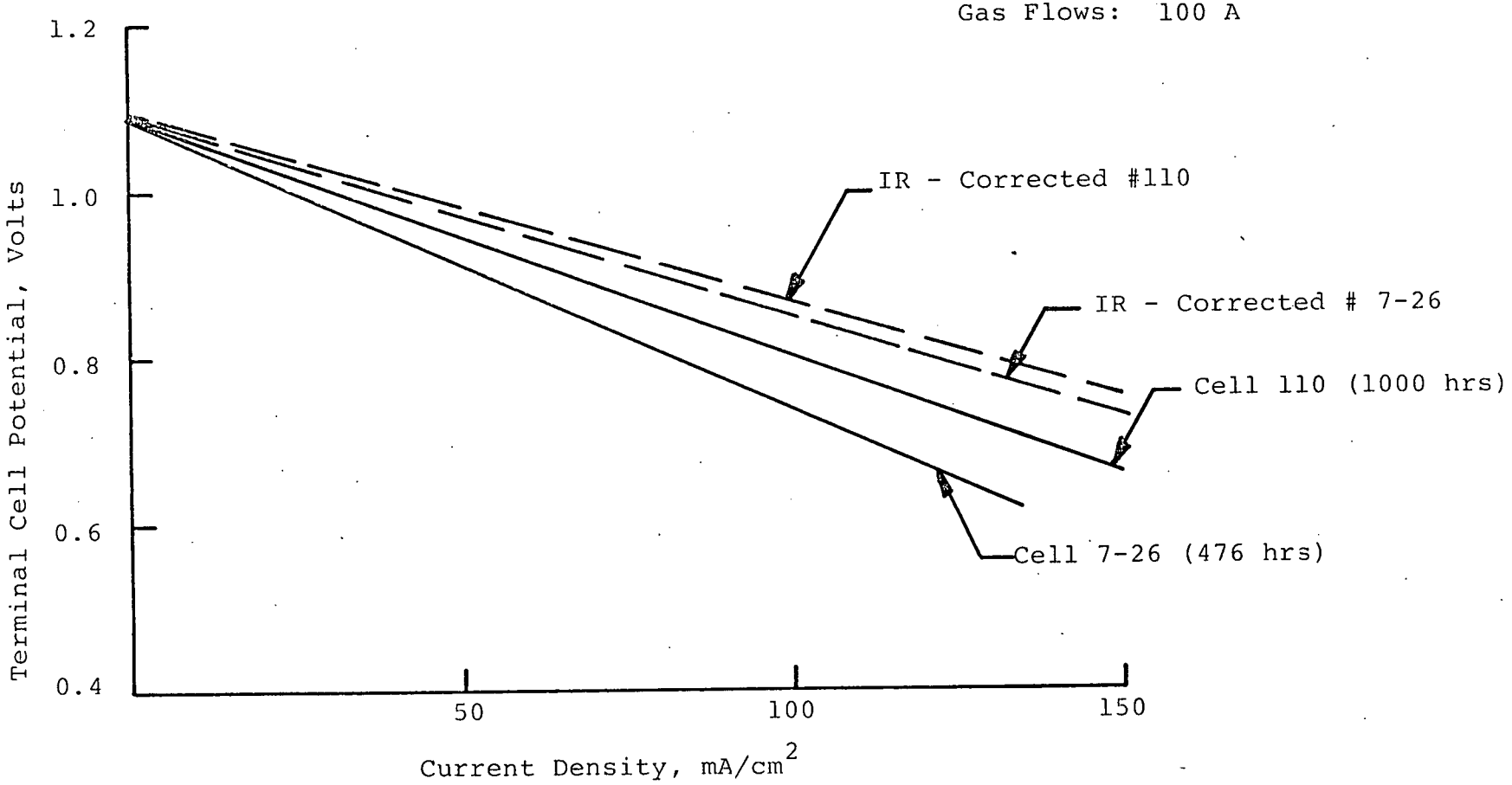

Figure 2.2.2 Scale up of a Ni-Co Anode - Cells 110 and 7-26

Temperature: 650°C
Electrode Area: 271 cm^2
Anode Gas: 74.2% H_2, 18.5% CO_2
7.3% H_2O, 100A Flow
Cathode Gas: 15% O_2, 30% CO_2
55% N_2, 100A Flow

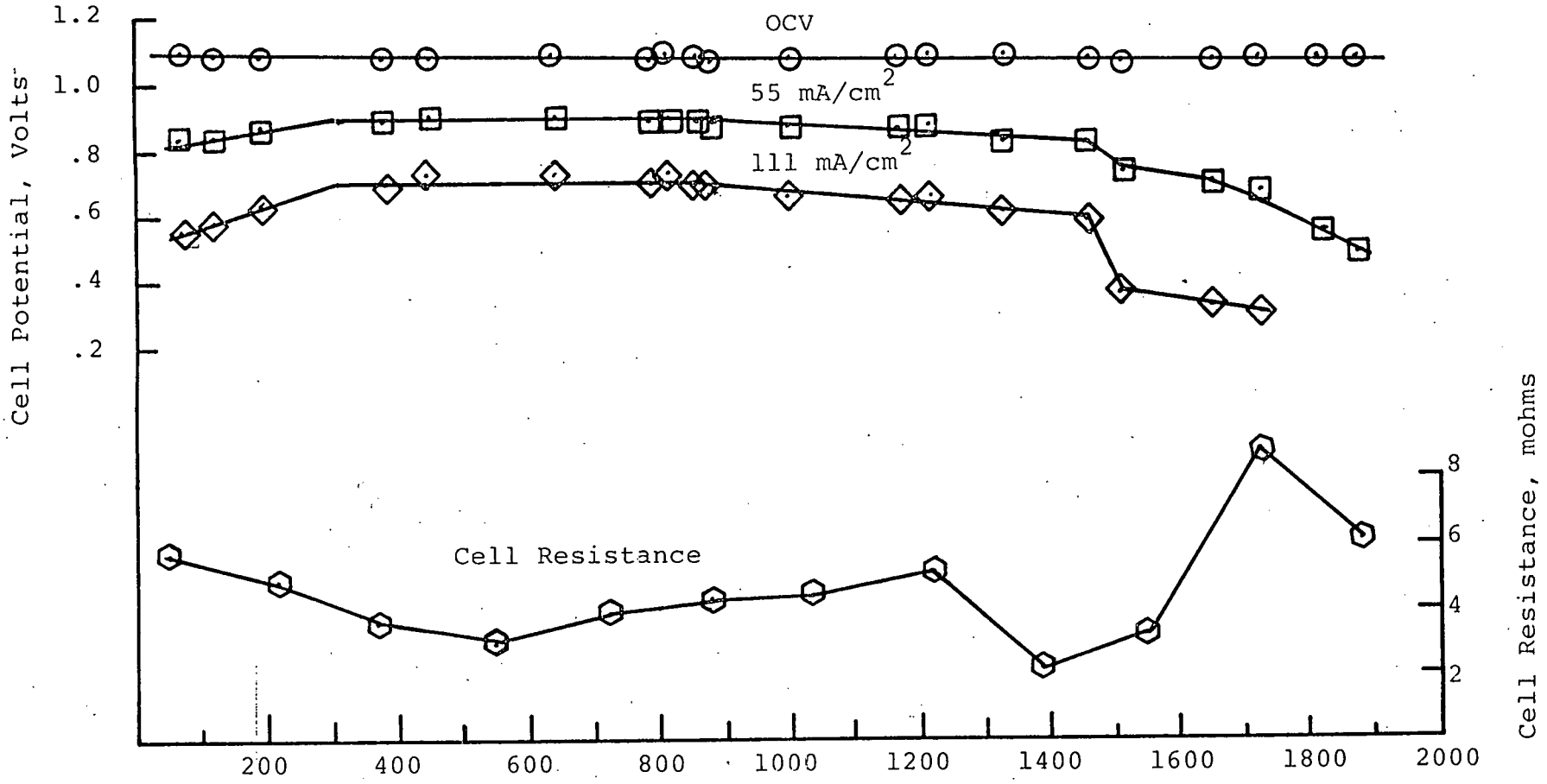

Figure 2.2.3: Endurance Testing of Lightweight Hardware - Cell S7-3

fabricated or procured. Testing of the pilot-size cells will start in the next quarter.

2.4 Diagnostics

During this quarter, post-test electrolyte inventory was performed for two 8.5 cm^2 size cells, Nos. 104 and 113, and one 300 cm^2 size cell, No. S7-2. Briefly, Cell 104 was an endurance test for nickel electrodes, Cell 113 a test evaluation of a new electrolyte batch prepared by a modified *in situ* method, and S7-2 a test of lightweight corrugated hardware. For specific details on these cells, the reader is refered to the ERC Quarterly Progress Report for April-June, 1978, (SAN/1169-9).

In addition to the electrolyte inventory, a Ni-Co anode was analyzed for its structural stability and Cell 113 was analyzed for phase stability of $LiAlO_2$.

2.4.1 Electrolyte Inventory Analyses

Post test electrolyte inventory is a useful diagnostic technique to evaluate anode/tile/cathode pore size compatibility and to determine electrolyte addition requirements. The electrolyte content in the porous cell components is measured by weight loss resulting from selective washing of the alkali carbonates. The results of such analyses on Cell Nos. 104, 113 and S7-2 are presented in Table 2.4.1. Using these data, the percent electrolyte lost from the system was calculated. The electrolyte distribution among the porous cell components at the termination of the test is presented in Table 2.4.2.

As seen in Table 2.4.1, Cells 104 and 113 appear to have lost electrolyte at a higher rate than Cell S7-2. A lower value of the electrolyte loss for S7-2 is a reflection of the smaller wet seal to active tile area ratio for 300 cm^2 cells. Furthermore, by comparing Cells 104 and 113, it seems that electrolyte loss didn't increase in proportion to cell

TABLE 2.4.1

ELECTROLYTE INVENTORY OF CELL 104, 113, and S7-2

DESCRIPTION	104	113	S7-2
Cell Endurance, hours	3100	1600	1400
Initial Mass of Electrolyte in Tile, g	3.04	3.38	75.36
Amount of Electrolyte Stored, g	-	0.1	-
Amount of Electrolyte Added During Cell Endurance, g	0.99	0.63	-
Mass of Electrolyte in Post-test Anode, g	0.075	0.003	0.092
Mass of Electrolyte in Post-test Cathode, g	0.367	0.081	4.98
Mass of Electrolyte in Post-test Tile, g	1.7	2.26	61.3
Mass of Electrolyte Lost from the System, g	1.89	1.77	8.99
% Electrolyte Loss from the System = $\frac{\text{Total electrolyte lost}}{\text{Total electrolyte}}$ *	46.9	43.0	11.9

* Total Electrolyte Lost = Total Electrolyte - electrolyte in cell component

Total Electrolyte = Electrolyte initially present and electrolyte added

TABLE 2.4.2

ELECTROLYTE DISTRIBUTION IN THE ACTIVE CELL COMPONENTS

CELL NO.	ENDURANCE	AMOUNT OF ELECTROLYTE IN GRAMS	% OF PORE VOLUME OCCUPIED BY CARBONATES
104	3100	Anode - 0.075	24
		Cathode - 0.367	44
		Tile - 1.700	69
113	1600	Anode - 0.003	1
		Cathode - 0.081	17
		Tile - 2.260	82
S7-2	1400	Anode - 0.092	1
		Cathode - 4.980	20
		Tile - 61.300	-

life. This, as expected, suggests that initial loss rates are higher due to wetting and corrosion of fresh hardware surfaces. As understanding of the time dependency of electrolyte loss rate is important for establishing a corresponding electrolyte addition schedule, more data of this type will be accumulated and compared in the next report.

Post-test electrolyte distribution in the active cell components of Cell Nos. 104, 113 and S7-2 are presented in Table 2.4.2. It is clear from the data that the anodes of Cells 113 and S7-2 were dry at the termination. This can explain the drop in performance observed for these two cells while Cell 104 performance was almost constant. The cathode pore volume occupied by the three cells is in the range of 16-44% and O_2/CO_2 gains were in the range of 90-100 mV. This suggests that the cathodes were operating under flooded conditions. However, more data of this type will be accumulated to determine an optimum wetting level.

Note that Table 2.4.2 shows an empty pore volume of 31% for Cell 104. This could be the reason for the observed lower OCV and cross-leak of the cell during the last 1000 hours as described in the Quarterly Technical Progress Report (SAN/1196-8). Similarly, the tile of Cell 113 had an empty pore volume of 18% and also showed a cross-leak.

2.4.2 Stability of Ni-Co Anode

Table 2.4.3 compares structural stability of the nickel-cobalt anode from Cell 110 with the nickel anode of Cell 7-17. The nickel anode experienced large structural changes in 2000 hours of endurance. In contrast, the nickel-cobalt anode, even after a longer endurance test, showed no appreciable changes in the structural parameters such as surface area, porosity, mean pore size and thickness. This

TABLE 2.4.3

STABILITY OF NICKEL & NICKEL-COBALT ANODE

	NICKEL ANODE	NICKEL-COBALT ANODE
Test No.	7-17	110
Endurance, Hrs.	2,000	3,300
Thickness, Mils:		
Initial	26	25
Final	20	24-25
Mean Pore Size, μ		
Initial	7.3	2.6
Final	19.5	2.4
Porosity, %		
Initial	72	65
Final	48	62
Surface Area, m^2/g		
Initial	∿.1	0.31
Final	-	0.32

establishes the sintering resistance of the nickel-cobalt alloy anode.

2.4.3 Stability of $LiAlO_2$

Post Test Measurement on Cell 113: The operational stability of the $LiAlO_2$ used as electrolyte support in Cell 113 (electrolyte batch No. B-112) was determined by x-ray diffraction and S.E.M. before and after the cell operation. The x-ray diffraction results are presented in Table 2.4.4 and S.E.M. micrographs of the pre- and post-test $LiAlO_2$ are shown in Figures 2.4.1 and 2.4.2 respectively.

The x-ray results described in Table 2.4.4 indicate that transformation of β- to both α- and γ- occured during the 1600 hours of cell life. As discussed in the previous Quarterly Report (SAN/1196-9), similar phase transformation behavior has been observed in both the small cell (No. 103) and the intermediate-size cell (No. 7-21) tests.

The S.E.M. micrograph in Figure 2.4.1 indicates a good crystal formation of all three phases in the pre-test sample. The micrograph of the post-test sample (Figure 2.4.2) indicates an apparent decrease in the abundance of rod-like particles. This observation is in agreement with the x-ray results which indicate a decrease in the beta-phase content.

Comparison of Structural Changes in $LiAlO_2$: Structural changes in $LiAlO_2$ due to cell operation for three batches of electrolyte, Batch No. B-106 (used in Cell 7-17), No. B-108 (used in Cell 7-18) and No. B-109 (used in Cell 7-21), are being analyzed. The results will be presented in the next report.

TABLE 2.4.4

PHASE STABILITY OF $LiAlO_2$ of CELL 113

DESCRIPTION OF SAMPLE	PHASE COMPOSITION w/o			SURFACE AREA m^2/g
	%α	%β	%γ	
Initial $LiAlO_2$	27	61	12	2.81
Post Test $LiAlO_2$ from Tile (excluding wet-seal)	36	42	22	3.65
% Change	+33	-31	+83	+29.9

1907-6 3000X

Figure 2.4.1: Electron Micrograph of $LiAlO_2$ of B-112, prior to use in Cell 113. (27% α + 61% β + 12% γ)

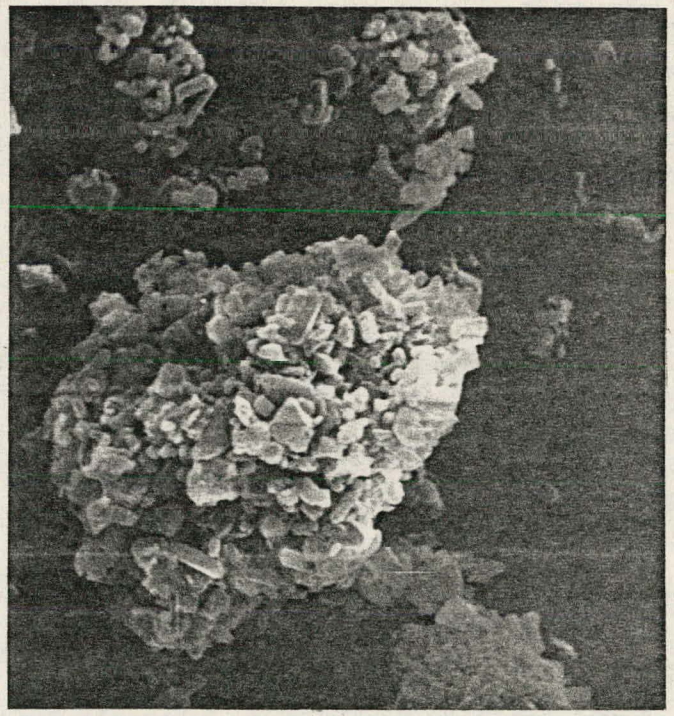

1934-6 3000X

Figure 2.4.2: Electron Micrograph of $LiAlO_2$ of B-112 after use in Cell 113. (36% α + 42% β + 22% γ)

TASK 3: STACK DESIGN AND DEVELOPMENT: J. Yasi, P. Patel, and D. Dharia

3.1 Sheet Metal Hardware Development

Evaluation of endurance stability of the lightweight corrugated sheet metal having a staggered pattern continued. This hardware, as described in Section 2.2, was tested in fuel Cell S7-3 for 1900 hours. The hardware was found intact with no appreciable corrosion. No significant structural changes were observed in the corrugated material for both anode and cathode sides. This confirms the observations made on the previous test Cell S7-2, as described in the previous report. We plan to use this material for the first lightweight stack test.

3.2 Lightweight Stack Testing

Design of various components of the first lightweight stack including a bipolar plate, end frames, manifolds, supports, and control panels has been completed. The bipolar plate has been designed to have minimum welding to keep thermal stresses at a minimum. The components are now being fabricated or procured. Testing will start next quarter.

TASK 4: MODELING AND SYSTEM ANALYSIS: D. Burns, P. Patel, and D. Dharia

4.1 Cell Performance Modeling

Compatibility of Electrodes: In the previous reports*, a preliminary comparision of cell performance was made for the cells having electrolyte tile made from the same batch and different pairs of electrodes. Performance of these cells was modeled for both noble oxidant and Air/CO_2 mixtures with the standard fuel gas composition. ECR (Equivalent Cell Resistance) results obtained for these cells using the Model MCFC1WG are compared in Table 4.1.1. The term OP (overpotential expressed in mΩ) is defined as ECR minus ohmic resistance (OR). Hence, this term represents polarizations at the anode and cathode.

As can be seen from Table 4.1.1, the cells having low surface area nickel anodes (Cell 104 and 111) yielded high values of the parameter OP for both the noble oxidant and the standard oxidant. The cells having high surface area nickel-cobalt anodes (Cells 110, 112 and 118) have comparatively lower values of the OP which explains their better performance.

As described in the last Quarterly Technical Progress Report (SAN/1196-9, Section 2.1), the performance of Cell 110 was improved by better selection of the cathode (Cell 112). As anticipated, modeling for these cells gave a lower value of OP with Air-CO_2 for the Cell 112 than that of Cell 110 and the same values of OP were obtained with O_2-CO_2.

Cell 118, having both anode and cathode made from nickel-cobalt alloy, displayed higher OP for Air-CO_2 than that of Cell 110 and 112. This can be explained by the relatively

---

*Technical Progress Reports SAN/1196-8 and SAN 1196-9, Section 2.1.

TABLE 4.1.1

MODELING STUDY OF COMPATIBILITY OF ELECTRODES[1]

CELL NO.	MEASURED OHMIC RESISTANCE, OR, mΩ	CATHODE GAS MIXTURE[2], 3A FLOWS			
		O_2-CO_2		Air-CO_2	
		ECR, mΩ	OP[3], mΩ	ECR, mΩ	OP[3], mΩ
104	86	275	189	324	238
111	82	249	167	306	224
110	68	184	116	231	163
112	49	163	114	188	139
118	86	190	104	257	171

1. All the cells have electrolyte tile hotpressed from Batch 108.
2. Anode Gas: 74.2% H_2, 18.5% CO_2, 7.3% H_2O; 3A flow
3. OP = ECR - OR

finer cathode in Cell 118 as compared to Cell 110 and 112.

Parallel Deviation Between Model and Experimental Data: The scheme presented in the earlier report (SAN/1196-9) to explain the parallel deviation between model and experimental data was further verified for Cell 104, 110 and 113.

As can be seen from Figure 4.1.1, modeling of Cell 110 using the model MCFC1WG resulted in a parallel deviation of 17 mvolts. Using the procedure described in the last report, this deviation was corrected. Further, using MCFC2WG, a good match for a value of 0.85 for effective mass transfer coefficient (K_e) was obtained as shown in Figure 4.1.1. Similarly, good matches were obtained for Cell 104 and 113 which established the validity of the procedure.

Electrolyte Distribution Modeling: To understand the electrolyte distribution among anode, cathode, and electrolyte tile, modeling work has been initiated. The model was proposed by H. Maru and L. Marianowski*. The main understanding that could be gained by this work is related to:

1) Optimization of anode and cathode inventory to reduce the concentration polarization

2) Improvement in compatibility of anode, cathode and tile pore structures

3) Establishing proper electrolyte inventory in the fuel cell to provide for the electrolyte losses and to obtain the minimum ohmic resistance

4) Understanding of a cross-leak due to the development of a through pore in the tile.

Two cells (Cell 7-17 and Cell 7-18) have been selected for the initial study. The results are being analyzed and

*Presented at 150th ECS Meeting, Las Vegas, Nevada, October 17-22, 1976

Cell No: 110
Cell Life: 91 hours
Cell Temperature: 650°C
Electrode Area: 8.56 cm^2
Anode Gas: 74.2% H_2, 18.5% CO_2
7.3% H_2O, 3A Flow
Cathode Gas: 66.7% CO_2, 33.3% O_2, 3A Flow

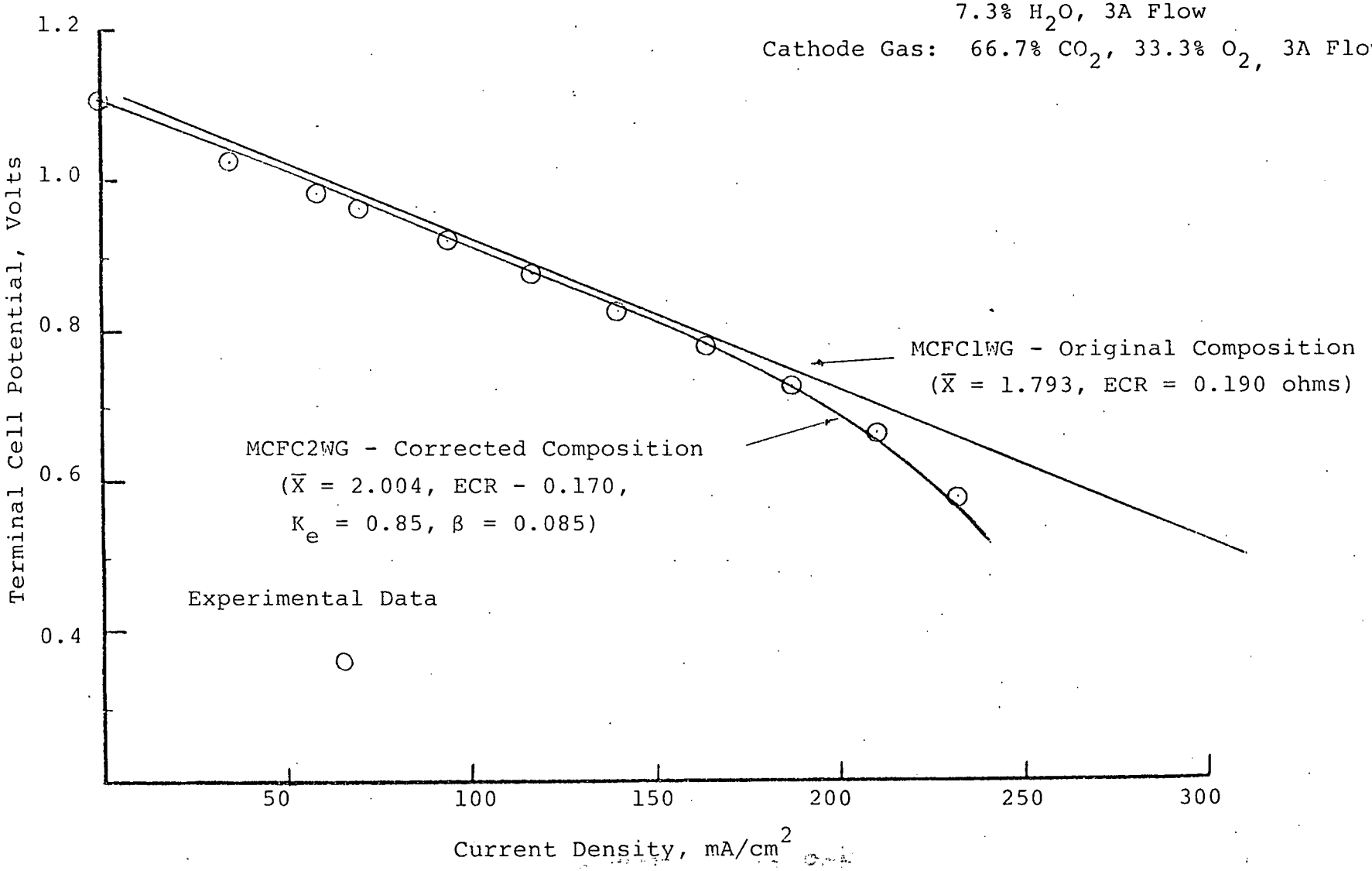

D0284

Figure 4.1.1; Modeling to Explain Parallel Deviation from Experimental Data

will be presented in the next report.

4.2 System Study

A system study on the Molten Carbonate Fuel Cell (MCFC) will be performed using a computer model for material and energy balances around the fuel cell stack and a cell performance model. The first model is described below, while the latter was described in our previous reports.

The system configuration is shown in Figure 4.2.1. The computer model for heat and energy balance is based on two considerations:

1) A catalytic burner is used to recycle CO_2 from anode to cathode, and

2) Heat generated in the stack is removed by ERC's DIGAS cooling method.

The term DIGAS represents DIstributed-GAS cooling which consists of dividing the cathode air in two streams--process air and cooling air. The process air flows through the cells supplying the reactants, O_2 and CO_2, whereas the cooling air flows through the cooling channels. The cooling air is not in contact with the electrolyte and its only function is to remove the heat generated in the stack.

For given compositions and utilizations on the fuel and the oxidant sides, and the operating parameters such as temperature and cell performance (cell voltage and current density), the computer model furnishes the material and energy balances. Some of the important results include electricity generated, waste heat available, recycle rate, cooling air flow rate, etc.

The above computer model requires cell performance to calculate heat generated in the cell. This can be computed

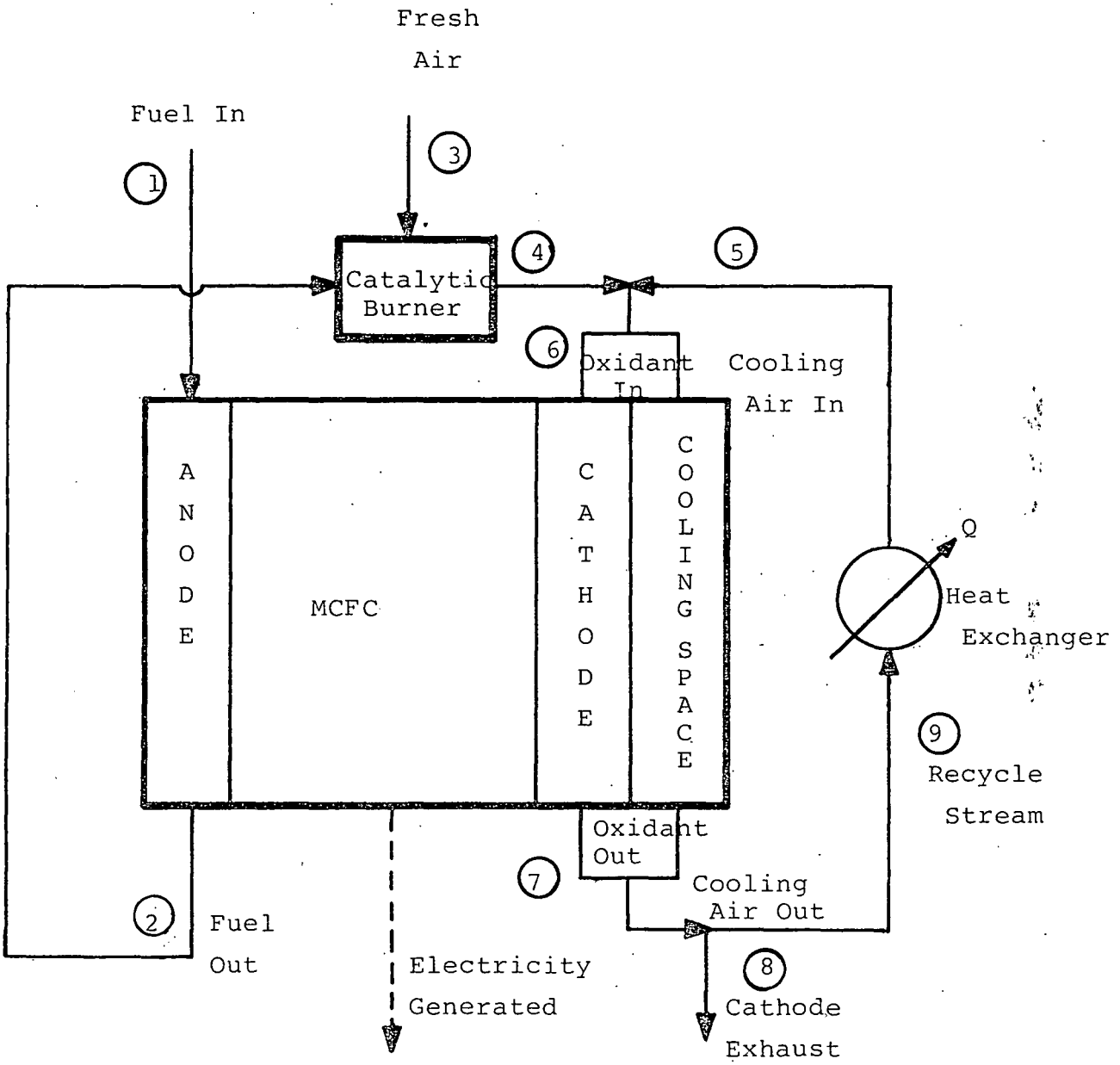

FIGURE 4.2.1: SCHEMATIC OF MCFC SYSTEM

by the MCFC performance model. But the MCFC performance model requires fuel and oxidant flow rates to start with. This makes it necessary to carry out an estimation of the cell performance and a computation of the material and energy balances in an iterative manner. Efforts are underway to modify the two computer models for their coupling with the material and energy balances. Once the entire package is ready, it will be used to carry out a parametric study of the MCFC system.

FUTURE WORK PLAN

In the next reporting period, efforts will be directed at the following tasks:

Component Development

Electrode manufacturing procedures will be modified to sinter thin plaques. Using the high surface area anode powder preparation, the effect of adding chromium to the nickel-cobalt alloy will be examined. Development of pilot-size electrode manufacturing procedures will be continued.

Pilot-size electrolyte tile manufacturing procedures will be improved to minimize thickness variations.

The wet-seal corrosion current measurements will be performed with 316 SS test coupons to examine the effects of gas composition as well as coating.

Cell Testing

The effect of electrolyte composition on cell performance will be examined. The lightweight sheet-metal hardware testing will be continued. Testing of a pilot-size cell will be initiated.

Stack Design and Development

Testing of a stack, assembled using lightweight sheet-metal frames, will begin towards the end of the next quarter.

Modeling and System Analysis

Electrolyte distribution modeling results will be analyzed. Using the system model, a parametric study of the MCFC system will be performed.

DISTRIBUTION LIST

	No. of Copies
Dr. John Ackerman Manager, Molten Carbonate Fuel Cell Program Argonne National Laboratory 9700 S. Cass Avenue D-205 Argonne, IL 60439	5
Dr. K. Kinoshita Chemical Engineering Division Argonne National Laboratory 9700 S. Cass Avenue Argonne, IL 60439	1
Dr. Alina Borucka Borucka Research Co. 60 Chestnut Street Livingston, NJ 07039	1
Prof. Ernest Yeager Case Western Reserve University University Circle Cleveland, OH 44106	1
Dr. J. Huff U. S. Army Mobility Equipment Research and Development Center Electrotechnology Branch Ft. Belvoir, VA 22060	1
Mr. Gary Voelker Assistant Director Power Systems Division U. S. Department of Energy 20 Massachusetts Avenue Washington, DC 20545	1
Mr. Martin Zlotnick U. S. Department of Energy 20 Massachusetts Avenue Washington, DC 20545	1
Mr. Richard Sperberg Co-ordinator San Francisco Operations Office U. S. Department of Energy 1333 Broadway Oakland, CA 94612	2
Mr. Arnold P. Fickett Electric Power Research Institute 3412 Hillview Avenue P. O. Box 10412 Palo Alto, CA 94303	1
Mr. E. Gillis Electric Power Research Institute 3412 Hillview Avenue P. O. Box 10412 Palo Alto, CA 94303	1
Dr. Theodore R. Beck Electrochemical Technology Corporation 3935 Leary Way N.W. Seattle, WA 98107	1
Mr. J. W. Harrison General Electric Company DECP 50 Fordham Road Wilmington, MA 01887	1
Dr. D. Chatterji, Manager Electrochemistry Branch General Electric Research & Development Center P.O. Box 8 Bldg. K-1, Room 2A54 Schenectady, NY 12301	1
Dr. J. Giner, President Giner, Incorporated 14 Spring Street Waltham, MA 02154	1
Mr. Leonard Marianowski Institute of Gas Technology 3424 S. State Street Chicago, IL 60616	1
Mr. Ron Guidotti Montana Energy and MHD Research & Development Institute Inc. Post Office Box 3809 Butte, MT 59701	1

DISTRIBUTION LIST

	No. of Copies
Dr. J. J. Rasmussen Montana Energy and MHD Research and Development Institute Inc. Post Office Box 3809 Butte, MT 59701	1
Dr. D. L. Johnson Technological Institute Department of Materials Science Northwestern University Evanston, IL 60201	1
Mr. Leslie M. Ferris Oak Ridge National Laboratory P.O. Box X Oak Ridge, TN 37830	1
Dr. Kurt Wray Physical Sciences, Inc. 30 Commerce Way Woburn, MA 01801	1
Dr. C. A. Trilling Atomics International Division Rockwell International 8900 De Soto Avenue Canoga Park, CA 91304	1
Mr. Leonard Nanis Stanford Research Institute 333 Ravenswood Avenue Menlo Park, CA 94025	1
Mr. R. D. Weaver Stanford Research Institute 333 Ravenswood Avenue Menlo Park, CA 94205	1
Mr. Joseph M. King Program Manager United Technologies Corporation P.O. Box 109 South Windsor, CT 06074	1